



HAL
open science

Very-long-period seismicity associated with the 2009–2015 reawakening of Cotopaxi Volcano, Ecuador

Indira Molina, Hiroyuki Kumagai, Mario Ruiz, Stephen Hernández, Patricia Mothes, Gabriela Arias, Joan Andújar

► **To cite this version:**

Indira Molina, Hiroyuki Kumagai, Mario Ruiz, Stephen Hernández, Patricia Mothes, et al.. Very-long-period seismicity associated with the 2009–2015 reawakening of Cotopaxi Volcano, Ecuador. *Journal of Volcanology and Geothermal Research*, 2024, 453, 10.1016/j.jvolgeores.2024.108150 . insu-04676492

HAL Id: insu-04676492

<https://insu.hal.science/insu-04676492v1>

Submitted on 9 Sep 2024

HAL is a multi-disciplinary open access archive for the deposit and dissemination of scientific research documents, whether they are published or not. The documents may come from teaching and research institutions in France or abroad, or from public or private research centers.

L'archive ouverte pluridisciplinaire **HAL**, est destinée au dépôt et à la diffusion de documents scientifiques de niveau recherche, publiés ou non, émanant des établissements d'enseignement et de recherche français ou étrangers, des laboratoires publics ou privés.



Distributed under a Creative Commons Attribution 4.0 International License

1 **Very-long-period seismicity associated with the 2009-2015**
2 **reawakening of Cotopaxi Volcano, Ecuador**

3
4 Indira Molina¹, Hiroyuki Kumagai², Mario Ruiz³, Stephen Hernández³, Patricia Mothes³, Gabriela
5 Arias⁴, Joan Andújar⁵

6
7 ¹Servicio Geológico Colombiano, Bogotá, Colombia cmolinap@sgc.gov.co

8 ²Nagoya University, Nagoya, Japan kumagai@eps.nagoya-u.ac.jp

9 ³Instituto Geofísico, Escuela Politécnica Nacional, Quito, Ecuador mrui@igepn.edu.ec,
10 pmothes@igepn.edu.ec, shernandez@igepn.edu.ec

11 ⁴Institut Géozur, Université Côte d'Azur arias@geoazur.unice.fr

12 ⁵ISTO, Orléans, France juan.andujar@cnrs-orleans.fr

13
14 *To be submitted to: Journal of Volcanology and Geothermal Research.*

15
16 **ABSTRACT**

17 Cotopaxi is a large, ice-capped stratovolcano located in the Ecuadorian Andes. After 72 years of
18 repose, Cotopaxi erupted on August 14, 2015. The precursory activity included long-period (LP)
19 events followed by volcano-tectonic (VT) earthquakes, very-long-period events accompanying LP
20 signals (VLP/LP events), tremor, deformation and SO₂ emissions. VLP/LP events were first
21 observed at Cotopaxi in 2002, and occurred persistently occurred from 2009 to 2014 and during
22 the 2015 eruptions. Previous studies of the VLP/LP seismicity suggested that these events
23 originated by repetitive volume changes in a crack due to degassing of water from magma at a
24 depth of 2–3 km beneath the NE flank. Based on this interpretation, we estimated the magma
25 volumes related to individual VLP/LP events from 2009 to 2015, which were systematically

26 extracted from continuous seismic records of the Cotopaxi broadband seismic network. Based on
27 the accumulated magma volume and the VLP/LP activity, our study is divided into seven periods
28 (phases A–G), during which the magma supply rate significantly fluctuated. In phase E (June 1–
29 July 27, 2015), before the eruptions, the magma supply rate increased. Degassing at the VLP source
30 generated gas flows in the conduit and pre-eruptive tremor, gradually drying out a shallow
31 hydrothermal system. In phase F (July 28–September 15, 2015), we estimated the highest magma
32 supply rate, leading to magma fragmentation at the VLP source and eruptions accompanied by
33 tremor. In phase G (September 16– December 29, 2015), the magma supply rate decreased, and
34 overall eruptive activity, VLP/LP events, and tremor gradually waned. These results indicate that
35 the VLP/LP events were likely generated by degassing from magma supplied to the VLP source
36 through an intruded dike before and during the eruptions. The VLP/LP activity provides critical
37 useful information about the magma supply rates that controlled eruptive and gas emission activity
38 at Cotopaxi during this period and may help to constrain magma volumes during future
39 reactivations.

40 **1. INTRODUCTION**

41 Cotopaxi (elevation 5876 m) is a large, ice-capped volcano, and one of the highest active
42 stratovolcanoes in the world. Cotopaxi is located south of Quito, Ecuador’s capital city of Ecuador,
43 and 40 km north of Latacunga (Fig. 1a). Its eruptive activity has been characterized by periodical
44 andesitic and rhyolitic eruptions (Hall and Mothes, 1995). Over the past 500 years, Cotopaxi has
45 experienced multiple cycles of eruptions in 1532–1534, 1742–1744, 1766–1768, 1853–1855,
46 1877–1880, 1903–1906, and 1942 (Coordinated Universal Time, UTC, is used throughout this
47 paper). During this period, there were 70 eruptions with Volcanic Explosivity Indices (VEIs) of

48 2–4, characterized by ash falls, as well as pyroclastic, debris and lava flows (Andrade et al., 2005,
49 Mothes et al., 1998; Hidalgo et al., 2018). Barberi et al. (1995) estimated the average recurrence
50 interval of eruptive episodes of Cotopaxi to be 117 years based on historical and stratigraphic
51 records over the last 2000 years. According to these historical records, smaller and less intense
52 eruptions, lasting months to years, preceded large eruptions (Hidalgo et al., 2018). Identifying pre-
53 eruptive signals before any unrest is crucial because of the population centers lying near the
54 volcano, and especially near lahar channels.

55
56 The Cotopaxi seismic network was deployed in 1989 and has been maintained and operated by the
57 Instituto Geofísico at the Escuela Politécnica Nacional (IG-EPN). It has recorded various seismic
58 signals, such as long-period (LP) events, tremor, volcano-tectonic (VT) earthquakes, very-long-
59 period (VLP) events accompanying LP signals (i.e., VLP/LP events), explosions, and ice quakes
60 in the summit glaciers (e.g., Ruiz et al., 1998; Metaxian et al., 2003; Molina et al., 2008; Kumagai
61 et al., 2010; Bernard et al., 2016; Hidalgo et al., 2018). According to the classification scheme of
62 Chouet (1996a), LP and VLP denote seismic events with frequency ranges of 0.5–5 Hz (0.2–2 s)
63 and 0.01–0.5 Hz (2–100 s), respectively. LP events display multiple oscillation cycles, while VLP
64 events often show one cycle, except for some unusual events reported at Mt. Erebus and Kilauea
65 (Waite, 2015). LP events are interpreted as acoustic vibrations of fluid-filled resonators in
66 magmatic and hydrothermal systems (e.g., Chouet, 1996b). VLP events are linked to mass transport
67 processes in magmatic and hydrothermal systems (e.g., Chouet and Matoza, 2013, and references
68 cited therein) related to magma intrusion and eruptive activity (e.g., Arciniega-Ceballos et al.,
69 1999; Molina et al., 2008; Maeda and Takeo, 2011; Park et al., 2020). VLP events exhibit high-
70 frequency signals at event onsets when they are associated with explosions (see Fig. 1d of Ripepe

71 et al., 2021). However, VLP events are not always associated with explosions or surface activity
72 (e.g., Hill et al., 2002; Marchetti and Ripepe, 2005). VLP/LP events at Cotopaxi show both VLP
73 and LP signatures (Molina et al., 2008).

74
75 Alternatively, tremor usually displays emergent onsets and dominant frequencies in the range of
76 0.066–10 Hz (0.1–15 s) (e.g., McNutt, 1992; Yukutake et al., 2017). The source processes of
77 tremor are interpreted as (i) flow-induced oscillations of conduit walls, (ii) successive cracking of
78 rocks due to injection of fluids, and (iii) hydrothermal interaction with magmatic gas and ash
79 emissions (Li et al., 2022 and references cited therein).

80
81 According to Ruiz et al. (1998), the seismic activity at Cotopaxi between 1989 and 1997 was caused
82 by the interaction between magmatic heat and the shallow hydrothermal system. During renewed
83 seismic activity in 2001–2003, VLP/LP events were observed at Cotopaxi for the first time between
84 June and September 2002 (Molina et al., 2008). Later, VLP/LP events from 2002 to 2015 were
85 reported by Molina et al. (2008), Kumagai et al. (2010), Arias (2016), and Anzieta et al. (2019).
86 VLP/LP sources were located below the NE flank of the volcano at a depth of 2–3 km (Molina et
87 al., 2008; Kumagai et al., 2010; Arias, 2016; Anzieta et al., 2019). During the seismic crisis from
88 2001 to 2003, Molina et al. (2008) reported on an increasing number of LP events in January 2001,
89 which were followed by a VT swarm in November 2001 and subsequent deformation beneath the
90 NE flank in or earlier than November 2001, prior to the appearance of fumarolic activity in early
91 January 2002 (Global Volcanism Program, 2002) (Fig. 2a). These changes led to the interpretation
92 of a magmatic intrusion beneath the NE flank. Continuing into late June 2002, impulsive VLP
93 signals accompanied by LP signals (i.e., VLP/LP events), characterized by a transition from non-

94 harmonic to harmonic oscillations were observed. VLP signals displayed a broad spectral peak of
95 around 0.5 Hz (2 s), and accompanied LP signals characterized by non-harmonic oscillations in
96 0.5–5 Hz (0.2–2 s) (see Figs. 3 and 6 of Molina et al., 2008). Molina et al. (2008) performed
97 waveform inversion of VLP signals and suggested that these VLP and LP signals were produced
98 by volume changes in the crack due to degassing of water at the top of an intruded magma and the
99 resonance of a crack filled with ash-laden gases released from the magma, respectively. The crack
100 was located beneath the NE flank at a depth of 2–3 km. Molina et al. (2008) also performed particle
101 motion analyses for the initiation onset (onset) portions of the VLPs events and found that these
102 events were located beneath the NE flank. Using waveform inversion analysis Kumagai et al.
103 (2010) estimated an inclined tensile crack mechanism for a VLP/LP event in 2009. This VLP/LP
104 event displayed impulsive VLP signals at its onset in a frequency band of 0.08 and 0.2 Hz (5–12.5
105 s), followed by LP signals consisting of non-harmonic oscillations with dominant peaks in 0.5–10
106 Hz (0.1–2 s) (see Figs. 4 and 5 of Kumagai et al., 2010). The source of this VLP event was located
107 at 2 km depth below the NE flank. In 2009, Cotopaxi's activity was accompanied by an increase
108 in LP events and sporadic SO₂ emissions of around 500 t/d (Bourquin et al., 2009). Small increases
109 in LP events also occurred in 2010 and 2011, and an active fumarole became more evident on the
110 western flank.

111
112 In early April 2015, a swarm of LP events was registered (Hidalgo et al., 2018; Gaunt et al., 2016),
113 peaking to 8–12 VLP/LP events per day in early May 2015 (Anzieta et al., 2019). On 4 June 2015,
114 LP activity transitioned to tremor characterized by broadband and non-harmonic oscillations,
115 which occurred almost continuously over the following two months (Hidalgo et al., 2018). This
116 tremor preceded a VT swarm, which then coincided with four phreatomagmatic eruptions with

117 VEI=2 on August 14 and 15, 2015 (Hidalgo et al., 2018; Bernard et al., 2016). These eruptions
118 were associated with numerous VLP/LP events (Anzieta et al., 2019) and tremor, which notably
119 increased on 21 August 2015 (Hidalgo et al., 2018). Ash emissions characterized the eruptive
120 activity that continued until the end of November 2015 (Bernard et al., 2016; Gaunt et al., 2016;
121 Hidalgo et al., 2018).

122
123 From 2001–2002, ground deformation was detected under the NE (Molina et al., 2008) and SW
124 flanks of the volcano, indicating magma migration from the SW to NE flanks along NNE–SSW
125 trending faults (Hickey et al., 2015). Morales Rivera et al. (2017) proposed that the observed
126 deformation between April and August 2015 resulted from an inclined sheet intrusion located a
127 few kilometers SW of the summit. The volume was estimated to be $6.8 \times 10^6 \text{ m}^3$, extending from
128 a depth of 12.1 km to 5.5 km below the summit. Based on petrological experiments, Martel et al.
129 (2018) proposed that the 2015 eruptions were fed by a continuous flux of magma with an average
130 water content of 3.5 wt%, originating from depths of 16 km to 7 km below the summit.

131
132 Aerial surveys conducted by IG-EPN revealed that the crater lake that existed before 14 August
133 2015 had disappeared, suggesting that the magmatic heat dried out water in the shallower system
134 (Gaunt et al., 2016). Hidalgo et al. (2018) estimated a magma volume of $65.3 \times 10^6 \text{ m}^3$ to supply
135 the emitted SO_2 gases during the 2015 eruptions. According to Bernard et al. (2016), the volume
136 of erupted materials was estimated to be $8.6 \times 10^5 \text{ m}^3$ based on the analysis of tephra falls. They
137 found that the amplitude variations of seismic tremors were correlated with the variations of ash
138 fallout mass emitted during the 2015 eruptions. Based on satellite images, Arnold et al. (2018)
139 estimated an erupted volume between 5×10^5 and $1.5 \times 10^6 \text{ m}^3$.

140

141 In this paper, we perform an analysis of VLP/LP events associated with the reawakening of
142 Cotopaxi Volcano during 2009–2015 (Fig. 2) to estimate the temporal evolution of the VLP/LP
143 activity and its relation to eruptive activity. Waveform inversion, as performed by Kumagai et al.
144 (2010), is the direct approach to quantifying VLP/LP sources. However, the VLP/LP event
145 analyzed by Kumagai et al. (2010) was the largest event during the studied period, and our
146 application of waveform inversion to other smaller events was unsuccessful due to low signal-to-
147 noise ratios in these signals. Therefore, we took another approach to estimate the source volumes
148 of the individual VLP/LP events by using their observed amplitudes. We assume that all the
149 VLP/LP events occurred at the same source location and with the same mechanism as those of the
150 largest VLP/LP event estimated by Kumagai et al. (2010). This assumption is justified by the
151 existence of a unique family of VLP/LP events in 2009–2015 as indicated by Anzieta et al. (2019)
152 and Arias (2016). Anzieta et al. (2019) employed unsupervised machine learning techniques in a
153 two-stage process to analyze seismic events using waveform data at station BREF (Fig. 1). Their
154 findings identified a unique family of VLP/LP events registered throughout 2015. This same study
155 also showed that VLP events disappeared during periods of heightened tremor activity and resurged
156 just before eruptions on August 14, 2015. Additionally, Arias (2016) applied a waveform cross-
157 correlation method to study waveform data at BTAM (Fig. 1). The result was an average cross-
158 correlation value of 0.8 between the largest VLP/LP event reported by Kumagai et al. (2010) and
159 VLP/LP events in 2009–2015, indicating that the same source repetitively triggered these VLP/LP
160 events.

161
162 We then estimated the magma volume related to the source of each VLP/LP event caused by H₂O
163 degassing following the interpretation of Molina et al. (2008). Accumulating these estimates, we
164 derived the temporal evolution of magma supply rate in 2009–2015. We found that a sharp increase

165 in magma supply rate occurred at the beginning of the 2015 eruptive activity. We also note that the
166 amplitudes and the daily number of VLP events were correlated with tremor amplitudes and SO₂
167 emissions during the eruptive activity. Based on these results and other observations, we discuss
168 the source processes of VLP/LP events and tremor and their implications for magmatic activity
169 before and during the 2015 eruptions at Cotopaxi Volcano.

170

171 **2. DATA**

172 A network of four permanent seismic stations equipped with 1 Hz seismometers was deployed in
173 1989 at Cotopaxi. The network was reinforced in 2001 by three additional permanent stations with
174 1 Hz seismometers and one temporal station featuring a seismometer with bandwidths of 0.2–40
175 Hz (Molina et al., 2008). In 2006, a joint project between the Japan International Cooperation
176 Agency (JICA) and IG-EPN (Kumagai et al., 2007; 2010) installed a seismic network (Fig. 1b) in
177 which each seismic station is comprised of a triaxial broadband seismometer (Güralp CMG-4T:
178 0.02–50 Hz). Seismic waveform data were digitized by a 24-bit data logger (Geotech Smart24D)
179 with a sampling frequency of 50 Hz at each station and then transmitted by a digital telemetry
180 system using 2.4 and 5 GHz wireless LAN to the central office of IG-EPN in Quito through
181 repeaters.

182

183 Waveform data acquired from the Cotopaxi broadband seismic network (Fig. 1b) was continuously
184 sampled and triggered by a detection system using filtered waveform amplitudes (Kumagai et al.,
185 2010). In this system, the maximum filtered waveform amplitudes using the latest one-minute files
186 were estimated. If the maximum amplitude at each station during the latest one-minute interval

187 exceeded a pre-established threshold, and if the number of triggered stations exceeded a pre-set
188 number, the waveform data were saved as an event for the latest three-minute-long files. Two
189 frequency bands for this detection trigger system were used: 0.3–2 Hz (LP band) and 0.02–0.1 Hz
190 (VLP band). These bands were empirically determined by performing tests for efficient triggering
191 of LP and VLP events at Cotopaxi by Kumagai et al. (2010). In this study, we observe that VLP/LP
192 events were triggered in the LP band because their amplitudes were larger in this band (Fig. A1).
193 The trigger level was set according to the noise level at each station. We used waveform data from
194 four broadband stations (BREF, BVC2, BTAM, and BMOR; Fig. 1b) to identify a long-term trend
195 in the VLP/LP activity. Due to poor data quality, waveform data at BNAS (Fig. 1b) were excluded.
196 BREF provided the highest quality data due to its proximity to the VLP/LP events, although this
197 station was occasionally affected by seismic signals from the descent of secondary lahars, mainly
198 occurring on the western flank after the eruption onset in August 2015. To examine the relationship
199 between VLP/LP events and tremor, we used the tremor data from Bernard et al. (2016) during the
200 2015 eruptive activity, which was derived from continuous waveform data at BREF. They manually
201 filtered out tectonic earthquakes to calculate the median and root mean square (RMS) amplitudes
202 of tremor signals. This process was performed using 10-minute sliding windows (without overlap)
203 in the 0.5–5 Hz band. We also generated similar tremor data in 2009–2015 using 1-day sliding
204 windows (without overlap) in the 0.5–5 Hz band. Using the solution for the moment source time
205 function of the largest VLP/LP event recorded at Cotopaxi on January 14, 2009 at 18:54 (Kumagai
206 et al., 2010), we calculated the magma supply rate as explained below (see Section 3.1).

207
208 Since 2008, SO₂ has been measured at Cotopaxi by two permanent scanning Differential Optical
209 Absorption Spectroscopy (DOAS) stations located 2.5 km north (REF) and 5 km west (NASA) of
210 the crater (Fig. 1b). Two additional stations were installed in 2015 (Hidalgo et al., 2018). The

211 processed data provided the mass emission of SO₂ in tons per month in 2009–2013 and the detailed
212 evolution in tons per day in 2015 (Hidalgo et al., 2018). Since 2010, IG-EPN has conducted
213 geodetic measurements using two surface and two borehole tiltmeters designed to detect small
214 ground deformation changes. From 2010 to 2015, the data acquisition procedures remained
215 unchanged, in which digital data were recorded every 5 minutes and simultaneously transmitted to
216 IG-EPN. Tiltmeters on the NE sector responded very well to magma ascent, and VC1 showed
217 notable changes (Fig. 1b). At VC1, a biaxial surface-mount tiltmeter is set on a cement base within
218 an old, well-settled massive lava. The summit glaciers are located 3.5 km upslope and have no
219 direct contact with VC1, which ensures that this tiltmeter has no relation to the changes in the
220 glacier thickness or melting. The distance from the VLP source to the tiltmeter is 6.1 km. Another
221 tiltmeter above the Refuge (close to REF DOAS station in Fig. 1b) also recorded moderate signals.

222

223 **3. METHODS**

224 **3.1 VLP/LP EVENT SELECTION AND AMPLITUDE DETERMINATION**

225 We used the catalog of LP and VLP events triggered by the automatic system between 2009 and
226 2015. From this catalog, we extracted the VLP/LP events by visually inspecting waveform plots
227 with 10-minute durations. According to Peterson (1993) and Webb (1998), the microseism falls
228 within the range of approximately 0.04–0.2 Hz (5–25 s). This microseism band overlaps with the
229 regional and teleseismic earthquakes and VLP events in a frequency band of approximately 0.04–
230 0.2 Hz. To distinguish a microseism from VLP/LP events, we followed the procedure proposed by
231 Dawson and Chouet (2014), which uses the power spectral density (PSD) for noise over 1 hour
232 before a VLP/LP event and the PSD for the same 1-hour length of both noise and VLP/LP signals.

233 Based on the spectral comparison, we determined that an amplitude larger than approximately 10^{-6}
234 m/s for VLP/LP events is a suitable threshold for selecting events in our catalog. To avoid
235 incorporating false VLP/LP events into our database, we eliminated events classified as regional
236 or teleseismic earthquakes by the Ecuadorian National Seismic Network of IG-EPN and USGS
237 catalogs. We then performed the following operations to select VLP/LP events with good signal-
238 to-noise ratios. After instrumental correction, vertical (UD) displacement seismograms were band-
239 passed between 0.08 and 1.0 Hz using a two-pole Butterworth filter to cut a time window of 30 s
240 for each VLP/LP event. This window consisted of 10 s before and 20 s after the maximum peak-
241 to-peak amplitude. We then selected VLP/LP events whose maximum amplitudes were three times
242 larger than the average amplitudes over the first 5 s (noise level). The time window was also applied
243 to the EW and NS components for each event at the same station. We manually deleted the events
244 with poor waveform features (i.e., pulses and noise). We determined the amplitude ratios of the
245 individual horizontal components to the UD component in a frequency band of 0.08–0.5 Hz and
246 estimated peak-to-peak amplitudes in the individual components. We chose the frequency band of
247 0.08–0.5 Hz because it produces larger amplitude signals within the range of our instrument
248 response (Fig. A1) and removes high-frequency signals affected by structural heterogeneities.

249

250 **3.2 VLP/LP EVENTS WAVEFORM FEATURES**

251 The vertical velocity seismograms and amplitude spectra observed at BREF for VLP/LP and LP
252 events are displayed in Fig. 3. The VLP/LP seismogram shows impulsive VLP signals with spectral
253 peaks in the frequency band of 0.2–1.6 Hz (0.63–5 s) with dominant peaks between 0.6 and 0.9 Hz
254 (1.11–1.66 s), which are accompanied by LP signals consisting of non-harmonic oscillations and
255 broad spectral peaks in the frequency band of 1.6–10 Hz (0.1–0.63 s) with dominant peaks between

256 2 and 4 Hz (0.25–0.5 s). VLP/LP events with similar spectral features occurred in 2002 (Molina et
257 al., 2008), 2009 (Kumagai et al., 2010), 2010–2014 (Arias, 2016), and 2015 (Anzieta et al., 2019).

258
259 Vertical velocity seismograms band-passed between 0.08 and 0.5 Hz for selected VLP events
260 observed at BREF between 2009 and 2015, show similar VLP waveforms throughout this period
261 (Fig. 4). This indicates that a single family of VLP events likely occurred at Cotopaxi Volcano, as
262 suggested by Anzieta et al. (2019) and Arias (2016). Higher frequency signals in the 1–5 Hz range
263 (as shown in Fig. 3b) appear in the VLP signals during the increased activity in 2009 and 2015.
264 Particle motion analysis by Arias (2016) and Anzieta et al. (2019) and waveform inversion analysis
265 by Molina et al. (2008) and Kumagai et al. (2010) revealed that the VLP sources are located at a
266 depth of 2–3 km beneath the NNE flank.

267

268 **3.3 SOURCE VOLUME REPRESENTATION**

269 A seismic source may be represented by the moment tensor, and the n -th component of the
270 displacement field is related to the moment tensor through the following equation (e.g., Aki and
271 Richards, 1980):

$$272 \quad u_n(\mathbf{x}, t) = M_{pq}(t) * G_{np,q}(\mathbf{x}, t), \quad (1)$$

273 where t is time, \mathbf{x} is space, M_{pq} is the pq -th component of the moment tensor, $G_{np,q}$ is the spatial
274 derivative of Green's function, and $*$ denotes the convolution operation. In the frequency domain,
275 Eq. (1) is equivalently written as $u_n(x, \omega) = M_{pq}(\omega)G_{np,q}(x, \omega)$, where ω is the angular
276 frequency. Based on the waveform inversion results of Kumagai et al. (2010), the most appropriate
277 seismic source to account for the largest VLP event at Cotopaxi is a tensile crack, for which the
278 moment tensor (\mathbf{M}) can be written as follows (e.g., Chouet, 1996b):

279
$$\mathbf{M} = s(t) \begin{pmatrix} \lambda/\mu + 2\sin^2\theta\cos^2\theta & 2\sin^2\theta\sin\phi\cos\phi & 2\sin\theta\cos\theta\cos\phi \\ 2\sin^2\theta\sin\phi\cos\phi & \lambda/\mu + 2\sin^2\theta\cos^2\phi & 2\sin\theta\cos\theta\sin\phi \\ 2\sin\theta\cos\theta\cos\phi & 2\sin\theta\cos\theta\cos\phi & \lambda/\mu + \cos^2\theta \end{pmatrix}, \quad (2)$$

280 where

281
$$s(t) = \mu\Delta V(t). \quad (3)$$

282 Here, θ and ϕ are the angles defining the normal direction of a crack, λ is Lamé's first elastic
 283 parameter, μ is Lamé's second elastic parameter or shear modulus, $s(t)$ is the source time function,
 284 and ΔV is the volume change of the crack (e.g., Chouet, 1996a). For the same crack angles (θ and
 285 ϕ) and elastic parameters (λ and μ), u_n in a frequency band is thus proportional to ΔV in this band,
 286 and the displacement amplitude ratios of EW/UD and NS/UD only depend on values of the crack
 287 angles.

288

289 We assume that the volume change in the crack is due to degassing of water from intruded magma
 290 (see Section 4.2). By applying the ideal gas law, we can calculate the mass of steam (M_g) associated
 291 with a VLP/LP event as follows:

292
$$M_g = \frac{\Delta V P_l}{\bar{R} T_m}, \quad (4)$$

293 where \bar{R} is the specific gas constant for steam, T_m is the magma temperature, and P_l is the pressure
 294 of the magma. M_g is related to magma volume (V_m) through the following equation (e.g., Taguchi
 295 et al., 2018):

296
$$V_m = \frac{M_g (1 - C_o)}{\rho_m (C_o - \sqrt{K_H P_l})}, \quad (5)$$

297 where C_o is the initial water content of the magma, ρ_m is the density of the liquid magma, and K_H
 298 is Henry's law constant. We assume the lithostatic pressure for P_l .

299

300 With reference to Section 4.1, the displacement amplitude ratios (EW/UD and NS/UD) of our
 301 analyzed VLP/LP events at the individual stations were almost constant, indicating that the crack
 302 angles did not change. Since the UD component is indisputable, we estimated the maximum
 303 amplitude of the vertical displacement seismogram (A_{ref}^j) in a frequency band of 0.08–0.5 Hz for
 304 the largest VLP/LP event analyzed by Kumagai et al. (2010) at the j -th station. Using the following
 305 approximation, we obtained the magma volume (V_{ij}^m) for the i -th VLP/LP event at the j -th station:

$$306 \quad V_{ij}^m = \frac{A_i^j V_m}{A_{ref}^j}, \quad (6)$$

307 where A_i^j is the maximum amplitude of the vertical band-passed displacement seismogram of the
 308 i -th VLP/LP event at the j -th station, and V_m is the magma volume estimated from the maximum
 309 amplitude of the source time function $s(t)$ for the largest VLP/LP event analyzed by Kumagai et
 310 al. (2010). We then summed the V_{ij}^m values to derive the accumulated magma volume and magma
 311 supply rate.

312

313 **4. RESULTS**

314 **4.1 VLP/LP EVENT AMPLITUDE EVOLUTION**

315 We observed maximum displacement amplitudes in the UD, EW, and NS components of the
 316 individual VLP/LP events within the frequency band of 0.08–0.5 Hz (2–12.5 s) at BREF, BTAM,
 317 BVC2, and BMOR. The temporal evolution of the UD amplitudes (Fig. 5) shows increases around
 318 January 14 and November 2, 2009, from early April to November 2011, early February to late July
 319 2012, early June 2015, late August, and mid-October 2015. However, the EW/UD and NS/UD
 320 ratios remained stable over the studied period (Fig. 5). This suggests that the crack angles did not

321 change during the VLP activity and supports our assumption that the displacement of either
322 component (UD, EW, or NS) is proportional to ΔV , i.e., the volume change. We selected the most
323 apparent UD value to calculate the magma volume estimates.

324
325 No data were recorded in 2009 at BTAM. Temporal changes in the UD amplitudes at BMOR in
326 2009 were smoother than those at BREF. The seismometer at BMOR is buried in unconsolidated
327 materials on a ridge at a remote location, about 6 km from the summit (Fig. 1b). In contrast, BREF,
328 located closest to the summit, is deployed on massive lava. Amplitude variability among these
329 stations may originate from such local site effects.

330

331 **4.2 MAGMA VOLUME ESTIMATES**

332 According to the VLP source estimates of Molina et al. (2008), Kumagai et al. (2010), Arias (2016),
333 and Anzieta et al. (2019), we assume magma emplacement at the VLP source occurred at a depth
334 of $h = 2500$ m (the average depth estimated by these studies) beneath the NNE flank. To determine
335 the magma volume at the VLP source, we employed Eqs. (3)–(6) as follows: $\mu = 10.6$ GPa for the
336 2500 m depth, which was derived from an S -wave velocity (β) of 2000 m/s and a rock density (ρ_s)
337 of 2650 kg/m³ (Molina et al., 2008). Incorporating the source time function $s(t)$ estimates
338 presented by Kumagai et al. (2010) for the largest VLP/LP event, we obtained a maximum value
339 of 6.32×10^{12} Nm. We then estimated ΔV for this event to be 596.2 m³. According to Martel et al.
340 (2018), recently erupted magma at Cotopaxi (primarily mafic andesite) was stored at depths
341 ranging from approximately 7 km to ≥ 16 km (with pressures from ~ 200 to ≥ 400 MPa) and
342 contained an average water content of 3.5 wt%. Since water is the most abundant volatile in magma
343 (Wallace, 2005), we assume that ΔV was caused by the degassing of water. Using a lithostatic

344 pressure (P_l) of 65 MPa, $\bar{R} = 462 \text{ J/ (K kg)}$, $T_m = 1223 \text{ K}$, and $\Delta V = 596.2 \text{ m}^3$, from Eq. (4), we
345 calculated $M_g = 6.85 \times 10^4 \text{ kg}$ for the largest VLP/LP event. Using Eq. (5), we estimated V_m for
346 this VLP/LP event to be $9.54 \times 10^3 \text{ m}^3$, assuming a water content (C_o) of 3.5 wt% in andesitic
347 magma with a density (ρ_m) of 2500 kg/m^3 and Henry's constant (K_H) of $1.6 \times 10^{-11} \text{ Pa}^{-1}$ (Nishimura,
348 2004). Using the V_m estimate, we computed V_{ij}^m values from Eq. (6). The A_{ref}^j values are listed in
349 relation to the individual stations (Table 1).

350
351 The accumulated amplitude and accumulated magma volume at BREF compared to tremor activity
352 are shown in Fig. 6a. Fig. A2 compares the accumulated magma volumes estimated at BVC2,
353 BTAM, and BMOR with those at BREF. Similar relative temporal changes are observed across all
354 stations, though BMOR shows the largest value (Fig. A2). As mentioned in the previous subsection,
355 these differences are likely attributable to site effects. Subsequently, we focused on estimates at
356 BREF. Based on the temporal variation in the accumulated magma volume (Fig. 6a) and the
357 individual VLP/LP amplitudes (Fig. 7a), we divided the VLP/LP activity into seven phases (A
358 through G) (Table 2). Specifically, we observe gradual increases in accumulated magma volume
359 between January 14 and September 18, 2009 (phase A) and between June 1 and July 27, 2015
360 (phase E), followed by sharp increases between September 19 and November 25, 2009 (phase B)
361 and between July 28 and September 15, 2015 (phase F), respectively (Figs. 6 and 7). The gradual
362 increase in phase E was associated with an increased number of LP events (Fig. 2c), elevated SO_2
363 emissions (Fig. 2e), and heightened tremor activity (Fig. 6a). In phase F, a significant number of
364 VLP/LP events occurred in August 2015 (about 200 events). Two phreatomagmatic explosions
365 associated with VLP/LP events took place on August 14–15, 2015, after which tremor reached its
366 peak during the studied period (Figs. 6a and 7a). Subsequently, the number of VLP/LP events

367 decreased in September 2015, and tremor associated with ash venting also decreased (Fig. 7a).
368 From September 7 until the end of November 2015 in phase G, VLP/LP and LP events, tremor, and
369 SO₂ emissions gradually decreased (Figs. 2, 6a, and 7).

370
371 From mid-February to mid-March 2010 and in April 2011, there were minor increases in the
372 accumulated magma volume. Therefore, we defined phase C as lasting from November 26, 2009,
373 to April 2011 (Fig. 6). From mid-September 2014, the accumulated magma volume again slightly
374 increased. Therefore, we defined phase D from April 2011 to May 2015 (Fig. 6a). The magma
375 supply rates varied significantly among the phases, with phase G's production being approximately
376 one order of magnitude smaller than those in other active periods (phases B, E, and F) (Table 2).

377 378 **4.3 VLP/LP EVENTS, TREMOR, ASH FALLOUT MASS, SO₂ EMISSION,**

379 **AND DEFORMATION**

380 Tremor amplitudes were correlated with the accumulated amplitudes of VLP/LP events during the
381 pre-eruptive, eruptive, and post-eruptive periods in 2015 (see phases E, F, and G in Fig. 6a, and
382 Table 2), where the VLP/LP accumulated amplitudes (i.e., magma supply rates) increased with
383 expanding tremor amplitudes. Before these periods, from 2009 to 2015, no evident relationship
384 between VLP/LP and tremor amplitudes was observed. However, it is noteworthy that tremor
385 amplitudes showed correlations with SO₂ emissions during this period (Figs. 2e and 6a). Bernard
386 et al. (2016) divided the eruptive activity in 2015 into 4 phases based on ash fallout mass, visual
387 observations, and tremor signal amplitudes. Phase 1 (August 14–15, 2015) was marked by the
388 opening of the conduit, which was associated with a major explosion on August 14, 2015 at 09:02,
389 followed by smaller explosions on the same day, generating plumes reaching 9.3 km above the

390 crater. Phases 2 (August 15–October 2, 2015), 3 (October 2–November 4, 2015), and 4 (November
391 4–30, 2015) were characterized by intense ash emissions. The magnitudes of these emissions
392 increased between phases 1 to 2 and later decreased over phases 2 to 4. These phases of Bernard et
393 al (2016) coincide with our phases F and G (Figs. 6b and 7). Pre-eruptive LP activity occurred from
394 early April to June 4, 2015 (Figs. 2a and 2c), followed by a registry of pre-eruptive tremor activity
395 from June 4 to August 13, 2015, during which phase E occurred (Fig. 6b).

396
397 Based on tremor activity, we defined peaks 1–4 in phases E and F (Fig. 7a). We also identified
398 peaks E and F based on the VLP/LP activity in phases E and F, respectively (Fig. 7a). We compared
399 the tremor amplitudes with the individual VLP/LP amplitudes and ash fallout mass (Fig. 7a), as
400 well as the daily number of VLP/LP events and SO₂ emissions (Fig. 7b). The number of daily
401 events and the amplitudes of VLP/LP events are highly correlated. Additionally, 45 days after the
402 onset of pre-eruptive tremor, we observe a close correlation between VLP/LP events, tremor, ash
403 fallout mass, and SO₂ emissions (Fig. 6b). This correlation substantiates the inception of phase E,
404 which reaches its peak on June 2, 2015 (Fig. 7a). After peak E, the VLP/LP amplitudes became
405 smaller during phase E until the end of July 2015. A fortnight later, phase F started with large
406 VLP/LP events, reaching peak F, which coincided with the first phreatomagmatic explosion on
407 August 14, 2015 at 09:02.

408
409 In summary, the eruptive activity in 2015 (Fig. 7a), particularly during peak F, exhibited the highest
410 daily number of VLP/LP events (Fig. 7b) and the most energetic VLP/LP activity when the conduit
411 system was opened. Subsequently, the VLP/LP amplitudes decreased during phase F, except for an
412 event that occurred on September 7, 2015, at 16:56 (Fig. 7a). In phase G, the VLP/LP activity
413 remained low, although a large event occurred on December 17 at 02:01 (peak G). It is notable that

414 this event took place after the eruptive activity had already ceased.

415

416 Prior to the eruptions, pre-eruptive tremor on June 2, 2015 (peak 1) and VLP/LP activity on June
417 6, 2015 (peak E) occurred before an SO₂ emission of ~4500 t/d on June 14, 2015 (Fig. 7b). On July
418 14, 2015, there was another SO₂ emission peak of ~5000 t/d (Fig. 7b). This peak was not linked to
419 either VLP/LP or tremor activity, and SO₂ emission then decreased gradually (Fig. 7b). The high
420 VLP/LP activity on August 13, 2015, occurred before the opening of the conduit (phase 1) with
421 the first explosion on August 14, 2015 at 9:02 (peak F), increased tremor activity, and an SO₂
422 emission peak of ~7200 t/d on August 15, 2015 (Fig. 7b). Following the first eruption on August
423 14, 2015, VLP/LP events, tremor activity, and SO₂ emission sharply decreased, although tremor
424 activity peaked again on August 28, 2015 (peak 2) (Fig. 7a). SO₂ emission gradually increased to
425 reach the maximum peak of ~16000 t/d on October 12, 2015, which almost coincided with peak 3
426 of tremor activity (Fig. 7b). In phases 3 and 4, when the conduit system was open, tremor activity
427 and SO₂ emission showed similar tendencies (Fig. 7b). Therefore, our results suggest that there are
428 correlations among VLP/LP events, tremor activity, and SO₂ emission. Before the eruptions, large
429 VLP/LP events tended to occur before tremor activity peaks, which were followed by SO₂ emission
430 peaks. During the eruptions, particularly in phases 3 and 4, tremor activity and SO₂ emissions
431 occurred simultaneously with a small number of VLP/LP events.

432

433 We performed a time-frequency analysis using continuous seismic data at BREF. We divided one
434 day's data into 1080 windows (80 seconds each), over which the PSD was calculated in a frequency
435 range of 0.2–12 Hz. Fig. 6b shows the normalized PSD as a function of time (spectrogram) between
436 January and December 2015. The relatively large spectrum amplitudes in a frequency band of 2.9–
437 7.8 Hz in early April and early June 2015 correspond to pre-eruptive tremor, which contains several

438 frequency peaks around 2.9, 3.5, 4.6, 5.4, 6.5, and 7.5 Hz. During phase E, we observe low-
439 frequency peaks around 0.5, 0.6, 0.8, 0.9, and 1 Hz of VLP/LP events, as well as the higher
440 frequency peaks of tremor signals. A peak frequency of 2.9 Hz gradually decreased to 2.1 Hz in
441 phase E, but other peaks remained stable (Fig. 6b).

442
443 Tiltmeter records (tangential and radial components to the summit crater) at VC1 (Fig. 1b) are
444 compared with the daily number of VLP/LP events in Fig. 8. Cyclic variations with amplitudes of
445 approximately 100 μ rad were observed each year from late 2010 to early 2015, attributed to
446 seasonal changes in groundwater and temperature. Significant deformation exceeding the seasonal
447 changes, particularly in the radial component, began to occur from April 10–25, 2015, coinciding
448 with the onset of pre-eruptive LP activity and continued until the peak of VLP/LP activity on June
449 19, 2015. Then, the deformation gradually decreased in phase F, during which the intensive
450 eruptions occurred. The largest peak of the VLP/LP activity was reached on August 25, 2015 (peak
451 F, Fig. 7a). No clear, convincing deformation signals associated with the VLP/LP activity were
452 detected by seven GPS stations on the volcano in 2015 (Mothes et al., 2017). The depth of the
453 deformation source has not been estimated. Molina et al. (2008) also observed deformation of the
454 NE flank prior to the appearance of the VLP/LP events from 2001 to 2003.

455

456 **5. DISCUSSION**

457 We interpret the VLP/LP and tremor activity at Cotopaxi from 2009 to 2015 as follows. The
458 VLP/LP events were generated by degassing of water from magma supplied at the crack source at
459 a depth of 2–3 km below the NNE flank of the volcano (Molina et al., 2008; Kumagai et al., 2010;

460 Arias, 2016; Anzieta et al., 2019). Our results indicate that the magma supply rates fluctuated
461 significantly from 2009 to 2015 (Fig. 6b and Table 2). The magma rate during the eruption activity
462 in 2015 (phase F) was higher than during the activity periods in 2009 (phases A and B), when no
463 eruptions occurred (Table 2). The continuous supply of magma through an intruded dike and
464 degassing at a depth of 2–3 km caused volume changes in a crack, leading to its resonances, which
465 were observed as VLP/LP events (Fig. 9a). When the magma supply rate was less than $10^{-2} \text{ m}^3/\text{s}$,
466 degassing and resultant bubble growth were not intensive, and no eruptions occurred (Fig. 9a).
467 Subsequently, the crack was filled with a magma-gas mixture, and gas was gradually released
468 through the partly closed conduit. The degassed dense magma descended and generated magma
469 convection in the dike (e.g., Kazahaya et al., 1994) (Fig. 9a). At this stage, magma intrusion feeding
470 the crack may have caused pressure fluctuations, evidenced by slight increases in LP and VLP/LP
471 events (Figs. 2c and 2d), and resonances in a shallow conduit observed as tremor from 2009 to
472 June 4, 2015, and as pre-eruptive tremor from June 4 to August 13, 2015 (Fig. 9a). Although the
473 shallower magma system may have been partly closed (Fig. 9a), some gases could escape through
474 the conduit and generate periodic variations, seen as tremor fluctuations accompanied by SO_2
475 emissions from 2009 to 2014 (Figs. 2e and 6a). There was no evident relationship between VLP/LP
476 and tremor activities between 2009 and May 31, 2015 (Fig. 6a), during which no large magma
477 supply rates were estimated (Table 2). This suggests that the crack was not well connected to the
478 conduit during this period. Before, the eruptions degassing became relatively intense. At this stage,
479 large VLP/LP events preceded the increasing tremor activity (see the beginning of phase E in Fig.
480 7a), and subsequently, the amplitudes of tremor and VLP/LP events were well correlated (see phase
481 E in Figs. 6a and 7a). The NE flank deformation over seasonal variations was detected during this
482 period (Fig. 8). As the magma supply rate increased (phase F), bubble growth became more
483 intensive and resulted in fragmentation (Fig. 9b). At this stage, significant VLP/LP events again

484 preceded the increase in tremor activity, with tremor and VLP/LP amplitudes showing a strong
485 correlation (see phases 1 and F in Figs. 6a and 7a). The crack was filled with ash and gas, which
486 ascended in the conduit and produced ash emissions. Such flows in the conduit generated tremor
487 associated with eruptions. The fragmentation condition was reached in phase F (Fig. 7), during
488 which the maximum magma supply rate ($1.12 \times 10^{-2} \text{ m}^3/\text{s}$) was estimated (Table 2). The intruded
489 dike was located in the source region of VT events (Ruiz et al., 1998) and may have been connected
490 through NNE–SSW fault systems to a magma reservoir at depths of 4–5 km beneath the SW flank
491 (Hickey et al., 2015). This reservoir was probably fed by a deeper reservoir located at depths from
492 7 to ≥ 16 km (Martel et al., 2018). Distal GPS data suggest that the deepest reservoir is located at
493 a depth of ~ 24 km below the SE flank (Mothes et al., 2017).

494
495 In 2015, although VLP/LP events were smaller individually, they occurred more frequently,
496 indicating a higher magma supply rate. A VT swarm preceded the 2015 eruption, unlike in 2009.
497 Deformation and seismicity in 2001–2003 were due to a low influx of magma accumulation that
498 stalled beneath the surface. The 2009 activity also indicated a low influx of magma. Magma
499 intrusions can occur without significant surface deformation due to fracture systems
500 accommodating the magma (Puglisi et al., 2008). At Cotopaxi, NNE-SSW trending faults may
501 accommodate magma from deeper parts without causing a VT swarm. Low magma supply rates
502 can result in fewer VT earthquakes (McNutt, 2005; Poland et al., 2008). VT earthquakes, caused
503 by brittle responses to stress from magmatic fluid movement, are linked to dike intrusions (e.g.,
504 Toda et al., 2022). LP seismicity represents magma pathways from the dike-VT earthquake depth
505 to the surface. The crack-generating VLP/LP events at Cotopaxi are proposed to be located above
506 this dike intrusion.

507
508 Increased pre-eruptive LP activity occurred between April 1 and the end of May 2015 (Figs. 2c and
509 6b). During this period, significant deformation occurred on the NE flank (Fig. 8). Due to limited
510 data, estimating the geometry and exact location of the deformation source is not possible; however,
511 we interpreted the deformation as being caused by an inflationary source beneath the NE flank,
512 which occurred in or before April 2015. This coincided with a significant increase in the number
513 of LP events (Figs. 2a and 2c) and a rise in VLP/LP events at the end of May 2015 (Figs. 2a and
514 2d). This behavior of deformation preceding VLP/LP events was also observed by Molina et al.
515 (2008) during the seismic crisis at Cotopaxi in 2001–2003. In May 2015, IG-EPN reported intense
516 fumarolic activity at the summit crater. Large VLP/LP events on June 1–2, 2015 (peak E) were
517 followed by pre-eruptive tremor on June 4, 2015 (Figs. 6b and 7). As the magma supply rate
518 gradually increased in phase E (Fig. 6a), pre-eruptive tremor reached its maximum amplitude on
519 June 6, 2015 (peak 1 in Fig. 7), and the deformation peaked on June 8, 2015, 7 days after the start
520 of phase E (Fig. 8). As the tremor amplitude decreased, its dominant peak frequency changed from
521 2.9 to 2.1 Hz from June 6 to August 13, 2015 (Fig. 6b), which may be caused by variations in gas
522 flows in the conduit (e.g., Yukutake et al., 2017). Hot gases passing through the partially closed
523 conduit gradually heated the shallow hydrothermal system (Fig. 9a); eventually, the water reached
524 its boiling point, causing the hydrothermal system to dry out gradually. Then, SO₂ gas emission
525 became active, reaching 4500 t/d on June 14, 2015 after peaks E and 1 (Fig. 7b). The peak of
526 VLP/LP events occurred 8 days before the peak of SO₂ emissions. The appearance of sulfide
527 deposits and a green-colored lake in the summit crater during the last week of July 2015 (Gaunt et
528 al., 2016) resulted from the interaction between magmatic gases and hydrothermal water provided
529 by the melting of the summit glacier. Gaunt et al. (2016) found that hydrothermal minerals such as
530 opal and alunite were emitted during the first phreatomagmatic explosions. These explosions were

531 caused by bubbly magma ascending through the conduit and coming into contact with
532 hydrothermal water.

533
534 The large VLP/LP event on August 14, 2015 at 9:02 (peak F in Fig. 7a) and another event at 9:07
535 on the same day partially cleared the conduit (Bernard et al., 2016). Plumes of explosions
536 associated with these events reached heights of ~7.8 km above the crater, and these eruptions were
537 followed by a peak in tremor amplitude (~900 a.u.) 6 minutes later (Fig. 7a). SO₂ emissions reached
538 ~7000 t/d on August 15. The peak of VLP/LP events occurred one day before the peak of SO₂
539 emissions and only six minutes before the onset of tremor related to the resonance of the conduit.
540 Two other explosions (August 15, 2015 at 15:45 and 21:02) finally cleared the entire conduit,
541 producing plumes that reached 9.3 km above the crater. These explosions on August 14 and 15,
542 2015 were classified as phreatic due to the scarcity of juvenile material (Gaunt et al., 2016) and
543 were accompanied by a small VT swarm. This opening of the system, evidenced by the large
544 explosions, likely improved connectivity between the crack and the conduit (Fig. 9b). On these
545 days, the peaks of VLP/LP and tremor amplitudes and SO₂ emissions occurred almost
546 simultaneously. Hidalgo et al. (2018) propose that this was due to the hydrothermal system being
547 superheated and decompressed. At this stage, we believe the conduit had a direct link to the crater
548 (Fig. 9b).

549
550 After the explosions on August 14–15, 2015, the relative amount of juvenile materials in ash
551 samples increased (Gaunt et al., 2016), suggesting faster magma ascent. This matches our estimate
552 in phase F, which shows the most abundant magma supply rate (Table 2). During this period, tremor
553 activity reached its maximum intensity on August 28, 2015 (peak 2 in Fig. 7a). According to Gaunt

554 et al. (2016), after the explosions on August 14–15, 2015, a thermal aureole developed around the
555 magmatic column, indicating drying processes in the hydrothermal system. At this stage, we
556 observed the stabilization of deformation, which may reflect the release of pressure within the
557 magma intrusion, possibly due to the opening of a conduit that allowed the escape of gases and
558 magma (see phase F in Fig. 8). As eruptions continued, juvenile grains transitioned to a greater
559 abundance of micro-crystalline materials due to slower magma ascent (Gaunt et al., 2016). This
560 also agrees with our estimate of a low magma supply rate in phase G (Table 2). The continued
561 stabilization of deformation (see phase G in Fig. 8) may be due to a decrease in the influx of magma
562 from greater depths. The variable crystal textures depending on magma supply rates are consistent
563 with those shown by Wright et al. (2012) for ash particles produced by eruptions at Tungurahua
564 volcano, Ecuador.

565
566 We estimated the total magma volume during the eruptive activity of phases F and G to be $5.4 \times$
567 10^4 m^3 (Table 2). It is one order of magnitude smaller than magma volumes of $\sim 8.6 \times 10^5 \text{ m}^3$ and
568 $3 \times 10^5 \text{ m}^3$ determined by field measurements of ash fallouts (Bernard et al., 2016) and deformation
569 data analysis (Arnold et al., 2018), respectively, during the eruptive activity. As shown in Fig. 7,
570 VLP/LP events were not always accompanied by tremor, and thus there existed eruptions without
571 VLP/LP events, which resulted in our smaller magma volume estimate (see phase 4 and the end of
572 phase G in Fig. 7a and Table 2). According to Morales Rivera et al. (2017) and Mothes et al. (2016),
573 magma volumes of $6.8 \times 10^6 \text{ m}^3$ and $(42 \pm 26) \times 10^6 \text{ m}^3$ at depths of 12–13 km and 24 km,
574 respectively, caused the deformation of the volcanic edifice before the 2015 eruptions. Hidalgo et
575 al. (2018) concluded that only 2–6 wt% of the magma supply to the reservoir was emitted during
576 the eruptive activity, based on analyses of SO_2 emissions and comparisons with the results from

577 deformation, geological, and petrological studies (e.g., Mothes et al., 2016; Bernard et al., 2016;
578 Gaunt et al., 2016; Morales Rivera et al., 2017; Arnold et al., 2018). These results indicate that a
579 large amount of magma remains at depths of ~7–24 km.

580
581 Although the magma volumes estimated from the VLP/LP activity reflect a partial amount of
582 magma supplied to the conduit, our results indicate that the temporal variation in the accumulated
583 magma volume is useful to infer magma supply processes. During the eruptive activity, tremor is
584 more directly linked to magma volume, as indicated by Bernard et al. (2016). In addition, we found
585 that the increase in tremor activity was triggered by large VLP/LP events during pre-eruptive
586 periods (Fig. 7a). When the magma supply rate was large, the seismic sequence occurred in the
587 following order at Cotopaxi: LP events, VT swarms, VLP/LP events, and tremor. The time
588 difference among VLP/LP events, tremor, and SO₂ emission became shorter when the magma
589 supply rate was larger and the system was more open. When the magma supply rate was lower and
590 the magma system was more closed, tremor was related to the passive degassing of SO₂ emissions
591 (Figs. 2e and 6a).

592

593 **6. CONCLUSIONS**

594 We systematically analyzed broadband seismic signals observed at Cotopaxi volcano and estimated
595 magma volumes related to the individual VLP/LP events from their observed amplitudes in a
596 frequency band of 0.08–0.5 Hz (2–12.5 s) in 2009–2015. The VLP/LP events were hypothesized
597 to be generated by the degassing of water from magma supplied to the conduit. Based on the
598 accumulated magma volume and the VLP/LP activity, our studied period was divided into 7 phases

599 (A through G), during which the magma supply rate largely fluctuated. We found correlations
600 among VLP/LP events, tremor, deformation, SO₂ emissions, and other observations and interpreted
601 the renewed activity as follows. In phases A–D, between January 14, 2009 and May 31, 2015,
602 during which the magma supply rate was low, degassing and resultant bubble growth at the VLP
603 source were not intensive, and no eruptions occurred. In phase E (June 1–July 27, 2015) before the
604 eruptions, the magma supply rate increased, degassing was relatively intensive, and the resultant
605 gas flows in the conduit generated pre-eruptive tremor. Hot gases surging through the conduit
606 gradually heated and dried out the shallow hydrothermal system. In phase F (July 28–September
607 15, 2015), the magma supply rate sharply increased, resulting in magma fragmentation at the VLP
608 source. This produced the large VLP/LP event on 14 August 2015 and associated explosions with
609 tremor, which opened the conduit. The increased VLP/LP and tremor activity and SO₂ emissions
610 occurred almost simultaneously. In phase G (September 16–December 29, 2015), the magma
611 supply rate decreased and eruptive activity gradually waned. We estimated from the VLP/LP events
612 the total magma volume during the eruptive activity of phases F and G to be $5.4 \times 10^4 \text{ m}^3$, which
613 is one order of magnitude smaller than magma volumes estimated from field surveys of ash fallout
614 mass and deformation analysis.

615
616 The VLP/LP events that occurred before and during the eruptions provide a comprehensive view
617 of the renewed magmatic activity. VLP/LP events, tremor, and SO₂ emissions at Cotopaxi were
618 related through non-destructive and continuous processes. The time differences among VLP/LP
619 events, tremor, and SO₂ emissions may depend on the connectivity within the dike, crack, and
620 conduit system. The opening of Cotopaxi's conduit was gradually achieved before eruptions,
621 resulting in shorter time intervals.

622
623 A small magma input reduces the supply of SO₂ to the summit. This condition corresponds to the
624 stage of long-term passive degassing, characterized by periodic fluctuations of SO₂ and tremor
625 between January 2009 and June 4, 2015. Our results suggest that future volcanic unrest at Cotopaxi
626 may begin when the magma supply rate exceeds 10⁻³ to 10⁻² m³/s. VLP/LP activity is a useful
627 indicator to estimate the magma supply rate and monitor future magmatic activity initiated by a
628 large amount of magma remaining in Cotopaxi's reservoir.

629

630 **ACKNOWLEDGEMENTS**

631 We thank the members of the Instituto Geofísico de la Escuela Politécnica Nacional (IG-EPN) for
632 their continuous efforts to maintain the Cotopaxi monitoring network. We thank Benjamin Bernard
633 for providing tremor and ash fallout mass data. We would like to thank Monica Segovia, Silvana
634 Hidalgo, and Caroline Martel for their helpful comments. Comments from two anonymous
635 reviewers helped to improve the manuscript. This work is a contribution under the cooperation
636 between IG-EPN and SGC (reference #018) from 2014.

637

638 **REFERENCES**

- 639 Aki, K., Richards, P.G., 1980. Quantitative Seismology. Freeman, New York.
- 640 Arias, G., 2016. Estudio de las señales sísmicas de muy largo periodo del Volcán Cotopaxi.
641 Bachelor Thesis, National Polytechnic School, Quito, Ecuador. URL:
642 <https://bibdigital.epn.edu.ec/handle/15000/13739>.
- 643 Anzieta, J., Ortiz, H., Arias, G., Ruiz, M., 2019. Finding possible precursors for the 2015 Cotopaxi
644 Volcano eruption using unsupervised machine learning techniques. *Int. J. Geophys.* 2019,
645 6526898, 8 pages. <https://doi.org/10.1155/2019/6526898>.
- 646 Arnold, D.W.D., Biggs, J., Wadge, G., Mothes, P., 2018. Using satellite radar amplitude imaging
647 for monitoring syneruptive changes in surface morphology at an ice-capped stratovolcano.
648 *Remote Sens. Environ.* 209, 480-488. <https://doi.org/10.1016/j.rse.2018.02.040>.
- 649 Bernard, B., Battaglia, J., Proaño, A., Hidalgo, S., Vasconez, F., Hernandez, S., Ruiz, M., 2016.

650 Relationship between volcanic ash fallouts and seismic tremor: quantitative assessment of the
651 2015 eruptive period at Cotopaxi volcano, Ecuador. *Bull. Volcanol.* 78, 80.
652 <https://doi.org/10.1007/s00445-016-1077-5>.

653 Andrade, D., Hall, M., Mothes, P., Troncoso, L., Eissen, J.-P., Samaniego, P., Egred, J., Ramón, P.,
654 Rivero, D., Yepes, H., 2005. Los Peligros Volcánicos Asociados con el Cotopaxi. In: *Los*
655 *peligros volcánicos en Ecuador*, No. 3. Corporación Editora Nacional.

656 Arciniega-Ceballos, A., Chouet, B., Dawson, P., 1999. Very long-period signals associated with
657 vulcanian explosions at Popocatepetl Volcano. *Geophys. Res. Lett.* 26, 3013-3016.
658 <https://doi.org/10.1029/1999GL010756>.

659 Bourquin, J., Hidalgo, S., Arellano, S., Troncoso, L., Galle, B., Arrais, S., Vásconez, F., 2009. First
660 observations of intermittent, non-eruptive gas emissions of Cotopaxi volcano (Ecuador)
661 during a period of heightened seismicity. *Eos Trans. AGU* 90 (52), Fall Meet. Suppl., Abstract
662 V23D-2140.

663 Chouet, B., 1992. A seismic model for the source of long-period events and harmonic tremor. In:
664 Gasparini, P., Scarpa, R., Aki, K. (Eds.), *Volcanic Seismology*. Springer, New York, pp. 133-
665 156. https://doi.org/10.1007/978-3-642-77008-1_5.

666 Chouet, B.A., 1996a. New methods and future trends in seismological volcano monitoring. In:
667 Scarpa, R., Tilling, R.I. (Eds.), *Monitoring and Mitigation of Volcano Hazards*. Springer,
668 Berlin, pp. 23-97. https://doi.org/10.1007/978-3-642-61313-5_2.

669 Chouet, B., 1996b. Long-period volcano seismicity: its source and use in eruption forecasting.
670 *Nature* 380, 309-316. <https://doi.org/10.1038/380309a0>.

671 Chouet, B.A., Matoza, R.S., 2013. A multi-decadal view of seismic methods for detecting
672 precursors of magma movement and eruption. *J. Volcanol. Geotherm. Res.* 252, 108-175.
673 <https://doi.org/10.1016/j.jvolgeores.2012.11.013>.

674 Dawson, P., Chouet, B., 2014. Characterization of very-long-period seismicity accompanying
675 summit activity at Kilauea Volcano, Hawai'i: 2007-2013. *J. Volcanol. Geotherm. Res.* 278-
676 279, 59-85. <https://doi.org/10.1016/j.jvolgeores.2014.04.010>.

677 Gaunt, H.E., Bernard, B., Hidalgo, S., Proaño, A., Wright, H., Mothes, P., Criollo, E., Kueppers,
678 U., 2016. Juvenile magma recognition and eruptive dynamics inferred from the analysis of
679 ash time series: The 2015 reawakening of Cotopaxi volcano. *J. Volcanol. Geotherm. Res.* 328,
680 134-146. <https://doi.org/10.1016/j.jvolgeores.2016.10.013>.

681 Global Volcanism Program, 2002. Report on Cotopaxi (Ecuador) (Wunderman, R., ed.). Bull.
682 Global Volcanism Network 27:12. Smithsonian Institution.
683 <https://doi.org/10.5479/si.GVP.BGVN200212-352050>.

684 Hall, M., Mothes, P., 1995. Bi-modal nature of the eruptive history of Cotopaxi Volcano, Ecuador.
685 IUGG XXI General Assembly, Boulder, Colorado. Abstract p. A452.

686 Hickey, J., Gottsmann, J.H., Mothes, P., 2015. Estimating volcanic deformation source parameters
687 with a finite element inversion: The 2001-2002 unrest at Cotopaxi volcano, Ecuador. *J.*
688 *Geophys. Res. Solid Earth* 120(3), 1473-1486. <https://doi.org/10.1002/2014JB011731>.

689 Hidalgo, S., Battaglia, J., Arellano, S., Sierra, D., Bernard, B., Parra, R., Kelly, P., Dinger, F.,
690 Barrington, C., Samaniego, P., 2018. Evolution of the 2015 Cotopaxi eruption revealed by
691 combined geochemical and seismic observations. *Geochem. Geophys. Geosyst.* 19, 2087–
692 2108. <https://doi.org/10.1029/2018GC007514>.

693 Hill, D.P., Dawson, P.B., Johnston, M.J.S., Pitt, A.M., Biasi, G.P., Smith, K., 2002. Very-long-
694 period volcanic earthquakes beneath Mammoth Mountain, California. *Geophys. Res. Lett.*
695 29(10), 1370. <https://doi.org/10.1029/2002GL014833>.

696 Kazahaya, K., Shinohara, H., Saito, G., 1994. Excessive degassing of Izu-Oshima volcano: magma
697 convection in a conduit. *Bull. Volcanol.* 56, 207-216. <https://doi.org/10.1007/BF00302080>.

698 Kumagai, H., Nakano, M., Maeda, T., Yepes, H., Palacios, P., Ruiz, M., Arrais, S., Vaca, M.,
699 Molina, I., Yamashina, T., 2007. Enhancing volcano-monitoring capabilities in Ecuador. *Eos*
700 *Trans. AGU* 88, 245-246. <https://doi.org/10.1029/2007EO230001>.

701 Kumagai, H., Vaca, M., Palacios, P., Nakano, M., Maeda, T., Yepes, H., Molina, I., Arrais, S.,
702 Ruiz, M., Yamashina, T., 2010. Broadband seismic monitoring of active volcanoes using
703 deterministic and stochastic approaches. *J. Geophys. Res.* 115, B08303.
704 <https://doi.org/10.1029/2009JB006889>.

705 Li, K.L., Bean, C.J., Bell, A.F., Ruiz, M.C., Hernández, S., Grannell, J., 2022. Seismic tremor
706 reveals slow fracture propagation prior to the 2018 eruption at Sierra Negra volcano, Galápagos.
707 *Earth Planet. Sci. Lett.* <https://doi.org/10.1016/j.epsl.2022.117533>.

708 Maeda, Y., Takeo, M., 2011. Very-long-period pulses at Asama volcano, central Japan, inferred
709 from dense seismic observations. *Geophys. J. Int.* 185, 265-282. <https://doi.org/10.1111/j.1365-246X.2011.04938.x>.

711 Marchetti, E., Ripepe, M., 2005. Stability of the seismic source during effusive and explosive

712 activity at Stromboli Volcano. *Geophys. Res. Lett.* 32, L03307.
713 <https://doi.org/10.1029/2004GL021406>.

714 Martel, C., Andújar, J., Mothes, P., Scaillet, B., Pichavant, M., Molina, I., 2018. Storage conditions
715 of the mafic and silicic magmas at Cotopaxi, Ecuador. *J. Volcanol. Geotherm. Res.* 354, 74-
716 86. <https://doi.org/10.1016/j.jvolgeores.2018.02.006>.

717 McNutt, S.R., 1992. Volcanic tremor. In: *Encyclopedia of Earth System Science*. Academic Press,
718 San Diego, California, pp. 417-425.

719 McNutt, S.R., 2005. Volcanic Seismology. *Annu. Rev. Earth Planet. Sci.* 33, 461-491.
720 <https://doi.org/10.1146/annurev.earth.33.092203.122459>.

721 Metaxian, J.-P., Araujo, S., Mora, M., Lesage, P., 2003. Seismicity related to the glacier of
722 Cotopaxi Volcano, Ecuador. *Geophys. Res. Lett.* 30, 1483.
723 <https://doi.org/10.1029/2002GL016773>.

724 Molina, I., Kumagai, H., García-Aristizábal, A., Nakano, M., Mothes, P., 2008. Source process of
725 very-long-period events accompanying long-period signals at Cotopaxi Volcano, Ecuador. *J.*
726 *Volcanol. Geotherm. Res.* 176, 119-133. <https://doi.org/10.1016/j.jvolgeores.2007.07.019>.

727 Morales Rivera, A.M., Amelung, F., Mothes, P., Hong, S.-H., Nocquet, J.-M., Jarrin, P., 2017.
728 Ground deformation before the 2015 eruptions of Cotopaxi volcano detected by InSAR.
729 *Geophys. Res. Lett.* 44, 6607–6615. <https://doi.org/10.1002/2017GL073720>.

730 Mothes, P.A., Hall, M.L., Janda, R.J., 1998. The enormous Chillos Valley lahar: an ash-flow
731 generated debris flow from Cotopaxi Volcano, Ecuador. *Bull. Volcanol.* 59, 233–244.

732 Mothes, P., Nocquet, J.-M., Morales, A., Jarrin, P., Gaunt, H.E., Yopez, M., Viracucha, G., 2016.
733 Geodetic signature of 2015–16 unrest at Cotopaxi-Ecuador: Modeling of GPS data, a deep
734 magma source, synchronous seismic swarms and petrologic constraints. *Cities on Volcanoes-9,*
735 *At Puerto Varas, Chile, Volume: S3*.

736 Mothes, P.A., Ruiz, M., Viracucha, G., Ramon, P., Hernandez, S., Hidalgo, S., Bernard, B., Gaunt,
737 E., Jarrin, P., Yopez, M., Espin, P., 2017. Geophysical footprints of Cotopaxi’s unrest and minor
738 eruptions in 2015: An opportunity to test scientific and community preparedness. In: Gottsmann,
739 J., Neuberg, J., Scheu, B. (Eds.), *Volcanic Unrest. Advances in Volcanology*. Springer, Cham.
740 https://doi.org/10.1007/11157_2017_10.

741 Nishimura, T., 2004. Pressure recovery in magma due to bubble growth. *Geophys. Res. Lett.* 31,
742 L12613. <https://doi.org/10.1029/2004GL019810>.

743 Park, I., Jolly, A., Lokmer, I., Kennedy, B., 2020. Classification of long-term very long period
744 (VLP) volcanic earthquakes at Whakaari/White Island volcano, New Zealand. *Earth Planets
745 Space* 72, 92. <https://doi.org/10.1186/s40623-020-01224-z>.

746 Peterson, J., 1993. Observation and modeling of seismic background noise. USGS Technical
747 Report 93-322.

748 Poland, M.P., Miklius, A., Sutton, A.J., 2008. A seismic shift in the monitoring of volcanic unrest.
749 *Nat. Geosci.* 1(7), 539-540. <https://doi.org/10.1038/ngeo279>.

750 Puglisi, G., Branca, S., Mattia, M., Aloisi, M., Bonaccorso, A., Boschi, E., 2008. Ground
751 deformation patterns at Mt. Etna before, during, and after the July-August 2001 eruption. *J.
752 Geophys. Res. Solid Earth* 113(B7). <https://doi.org/10.1029/2006JB004791>.

753 Ripepe, M., Delle Donne, D., Legrand, D., Valadade, S., Lacanna, G., 2021. Magma pressure
754 discharge induces very long period seismicity. *Sci. Rep.* 11, 20065.
755 <https://doi.org/10.1038/s41598-021-99513-4>.

756 Ruiz, M., Guillier, B., Chatelain, J.L., Yepes, H., Hall, M., Ramon, P., 1998. Possible causes for
757 the seismic activity observed in Cotopaxi Volcano, Ecuador. *Geophys. Res. Lett.* 25, 2305-2308.
758 <https://doi.org/10.1029/98GL01514>.

759 Taguchi, K., Kumagai, H., Maeda, Y., Torres, R., 2018. Source properties and triggering processes
760 of long-period events beneath volcanoes inferred from an analytical formula for crack
761 resonance frequencies. *J. Geophys. Res. Solid Earth* 123, 7550-7565.
762 <https://doi.org/10.1029/2018JB015866>.

763 Toda, S., Stein, R., Sagiya, T., 2002. Evidence from the AD 2000 Izu islands earthquake swarm
764 that stressing rate governs seismicity. *Nature* 419, 58-61. <https://doi.org/10.1038/nature00997>.

765 Waite, G.P., 2015. Very-long-period seismicity at active volcanoes: source mechanisms. In: Beer,
766 M., Kougioumtzoglou, I.A., Patelli, E., Au, S.K. (Eds.), *Encyclopedia of Earthquake
767 Engineering*. Springer, Berlin, Heidelberg. https://doi.org/10.1007/978-3-642-35344-4_46.

768 Wallace, P.J., 2005. Volatiles in subduction zone magmas: concentrations and fluxes based on melt
769 inclusion and volcanic gas data. *J. Volcanol. Geotherm. Res.* 140(1-3), 217-240.
770 <https://doi.org/10.1016/j.jvolgeores.2004.07.023>.

771 Webb, S.C., 1998. Broadband seismology and noise under the ocean. *Rev. Geophys.* 36(1), 105-
772 142. <https://doi.org/10.1029/97RG02287>.

773 Woods, J., Donaldson, C., White, R.S., Caudron, C., Brandsdóttir, B., Hudson, T.S., Ágústsdóttir,

774 T., 2018. Long-period seismicity reveals magma pathways above a laterally propagating dyke
775 during the 2014-15 Bárðarbunga rifting event, Iceland. *Earth Planet. Sci. Lett.* 490, 216-229.
776 <https://doi.org/10.1016/j.epsl.2018.03.020>.

777 Wright, H.M.N., Cashman, K.V., Mothes, P.A., Hall, M.L., Ruiz, A.G., Le Pennec, J.-L., 2012.
778 Estimating rates of decompression from textures of erupted ash particles produced by 1999-
779 2006 eruptions of Tungurahua volcano, Ecuador. *Geology* 40(7), 619-622.
780 <https://doi.org/10.1130/G32948.1>.

781 Yukutake, Y., Honda, R., Harada, M., Doke, R., Sakai, S., Ueno, T., Morita, Y., 2017. Analyzing
782 the continuous volcanic tremors detected during the 2015 phreatic eruption of the Hakone
783 volcano. *Earth Planets Space* 69, 164. <https://doi.org/10.1186/s40623-017-0751-y>.

784 **TABLES**

785 **Table 1.** Maximum displacement amplitudes in a frequency band of 0.08–0.5 Hz of the largest
 786 VLP/LP event that occurred on January 14, 2009, at the individual stations (A_{ref}^j) and total
 787 accumulated amplitude and magma volume estimated from VLP/LP events from 2009 to 2015.

788

Station	A_{ref}^j (m)	Total accumulated amplitude (m)	Total accumulated magma volume (m ³)
BREF	5.96×10^{-5}	1.37×10^{-3}	2.19×10^5
BVC2	2.27×10^{-5}	3.38×10^{-4}	1.42×10^5
BMOR	1.33×10^{-5}	5.49×10^{-4}	3.94×10^5
BTAM	2.49×10^{-5}	3.80×10^{-4}	1.46×10^5
Average		6.59×10^{-4}	2.25×10^5

789

790

791 **Table 2.** Magma volumes and magma supply rates in the individual phases (A–G) estimated from
 792 the amplitudes in a frequency band of 0.08–0.5 Hz at BREF.

793

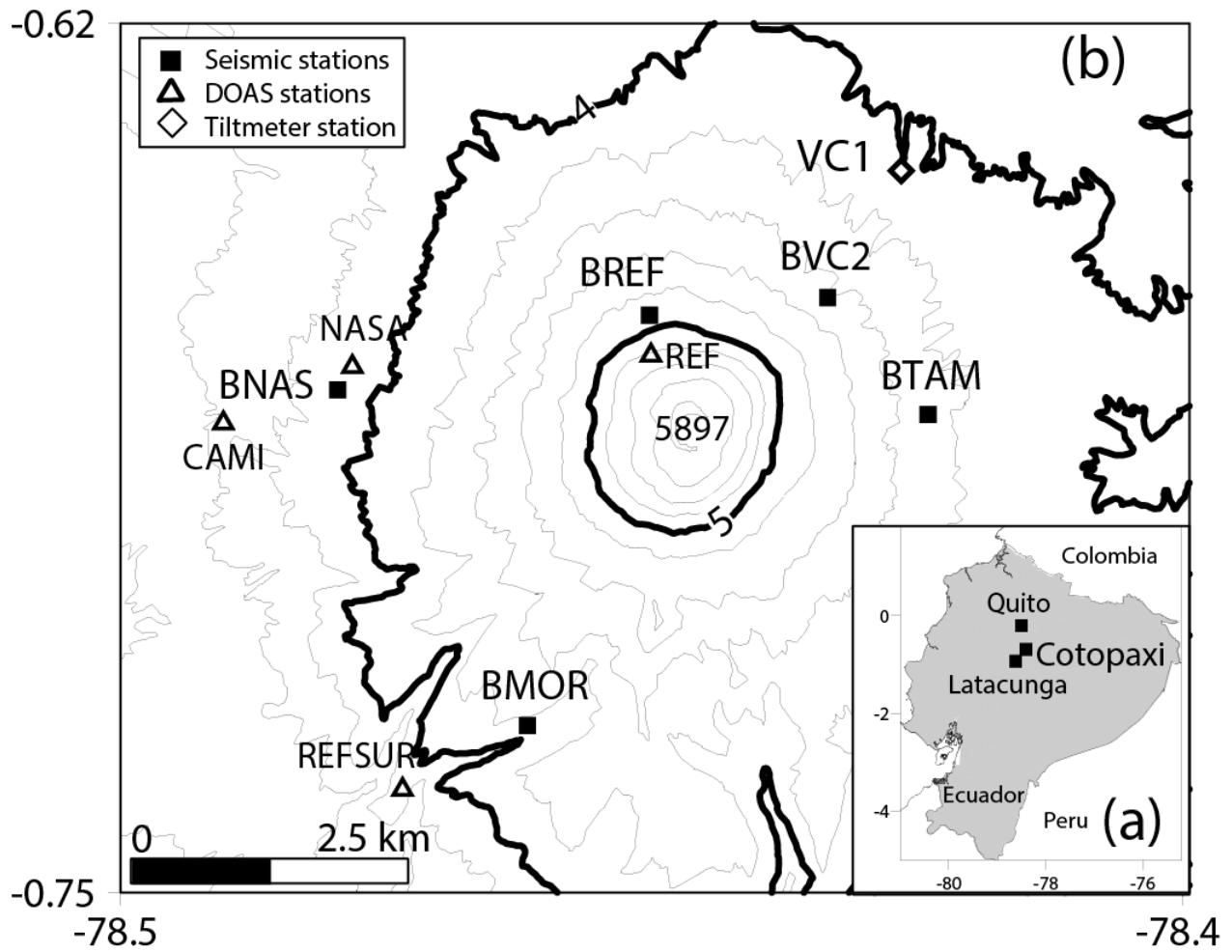
Phase	Start date	End date	Magma volume (m ³)	Magma supply rate (m ³ /s)
A	January 14, 2009	September 18, 2009	3.25×10^4	1.52×10^{-3}
B	September 19, 2009	November 25, 2009	4.73×10^4	8.17×10^{-3}
C	November 26, 2009	April 26, 2011	1.64×10^4	3.67×10^{-4}
D	April 27, 2015	May 31, 2015	3.63×10^4	2.81×10^{-4}
E	June 1, 2015	July 27, 2015	2.38×10^4	4.92×10^{-3}
F	July 28, 2015	September 15, 2015	4.72×10^4	1.12×10^{-2}
G	September 16, 2015	December 29, 2015	6.32×10^3	7.32×10^{-4}

794

795

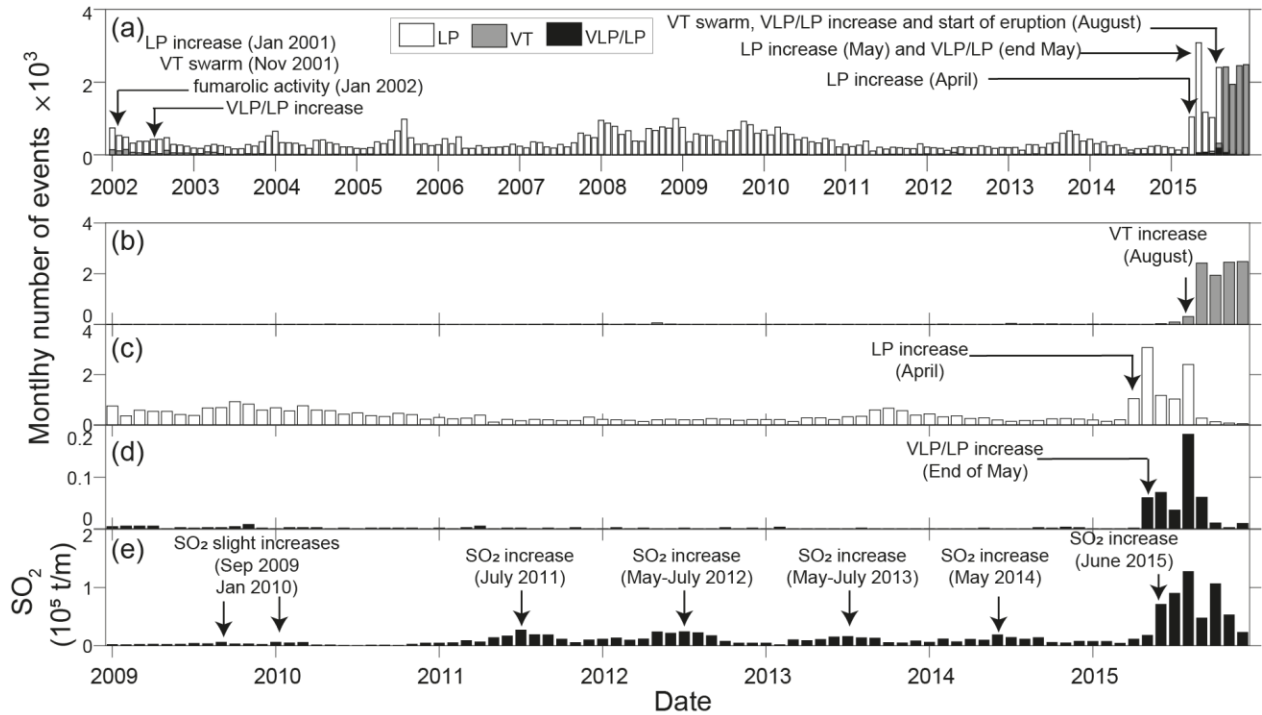
796 **FIGURES**

797



798

799 **Fig. 1.** (a) Location of Cotopaxi Volcano in Ecuador. (b) Topographic contours of Cotopaxi Volcano,
800 every 200 m, showing the locations of the seismic, DOAS, and tiltmeter stations.

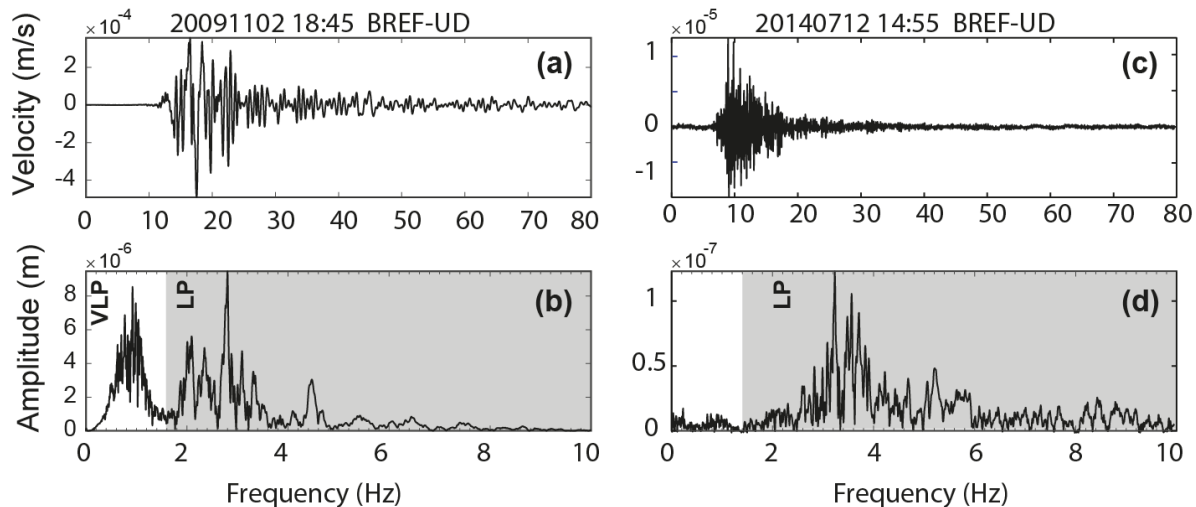


801

802 **Fig. 2.** Temporal variations in VLP/LP, VT, and LP activity and SO₂ gas emission. (a) Monthly
 803 numbers of LP, VT, and VLP/LP events from 2002 to 2015. (b, c, d, e) Monthly numbers of VT,
 804 LP, and VLP events and SO₂ emission (t/month), respectively, from 2009 to 2015. Vertical arrows
 805 in (e) display periods when SO₂ increased.

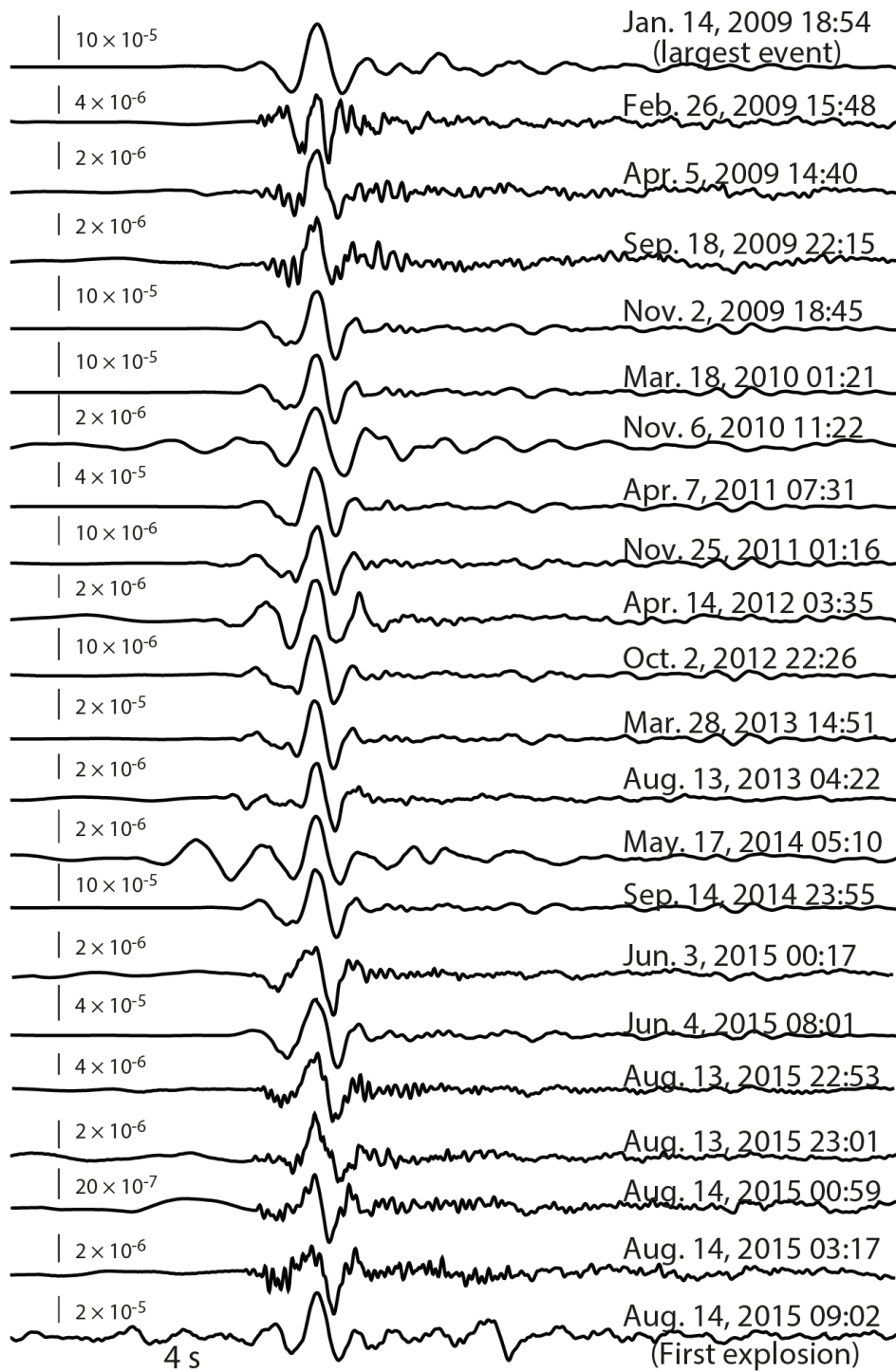
806

807

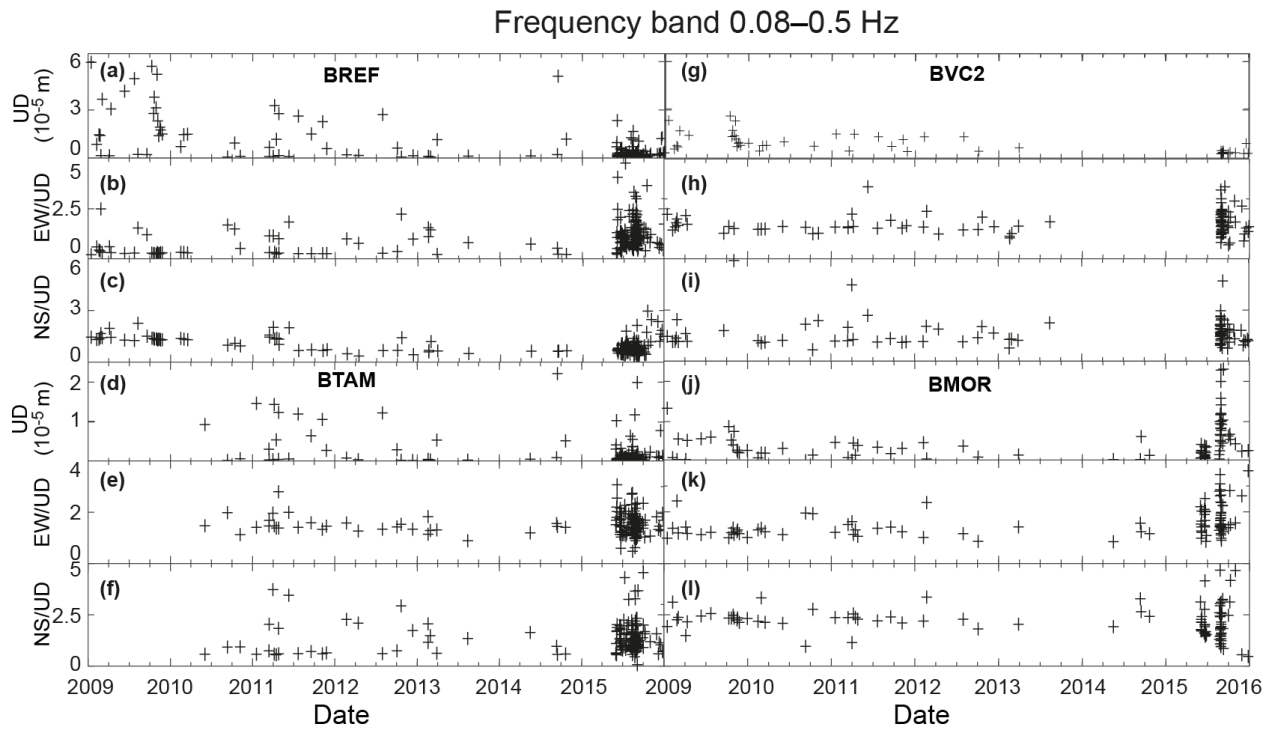


808

809 **Fig. 3.** Vertical waveforms and their spectra of (a, b) VLP/LP and (c, d) LP events at BREF. An LP
 810 band of 1.6–10 Hz (0.1–0.63 s) is indicated by gray in each spectrum, and a VLP band of 0.2–1.6
 811 Hz (0.63–5 s) is indicated by white in (b).



814 **Fig. 4.** Vertical velocity seismograms of VLP signals in VLP/LP events band-passed in a frequency
 815 band of 0.08–0.5 Hz at station BREF. Amplitude (m/s) is indicated by a vertical bar at the left of
 816 each seismogram. The first waveform is the largest VLP/LP event analyzed by Kumagai et al.
 817 (2010), which is our reference event to determine magma volume.



818

819 **Fig. 5.** Temporal variations in UD amplitudes and amplitude ratios of EW/UD and NS/UD of VLP
 820 signals in VLP/LP events in a frequency band of 0.08–0.5 Hz from 2009 to 2015. (a, b, c) BREF.
 821 (d, e, f) BTAM. (g, h, i) BVC2. (j, k, l) BMOR. The averages and standard deviations of the EW/UD
 822 ratios were 1.1 ± 0.7 , 1.5 ± 0.4 , 1.7 ± 0.5 , and 1.6 ± 0.6 at BREF, BTAM, BVC2, and BMOR,
 823 respectively. Those of the NS/UD ratios were 0.9 ± 0.4 , 1.3 ± 0.7 , 1.7 ± 0.9 , and 2.2 ± 0.8 at BREF,
 824 BTAM, BVC2, and BMOR, respectively.

825

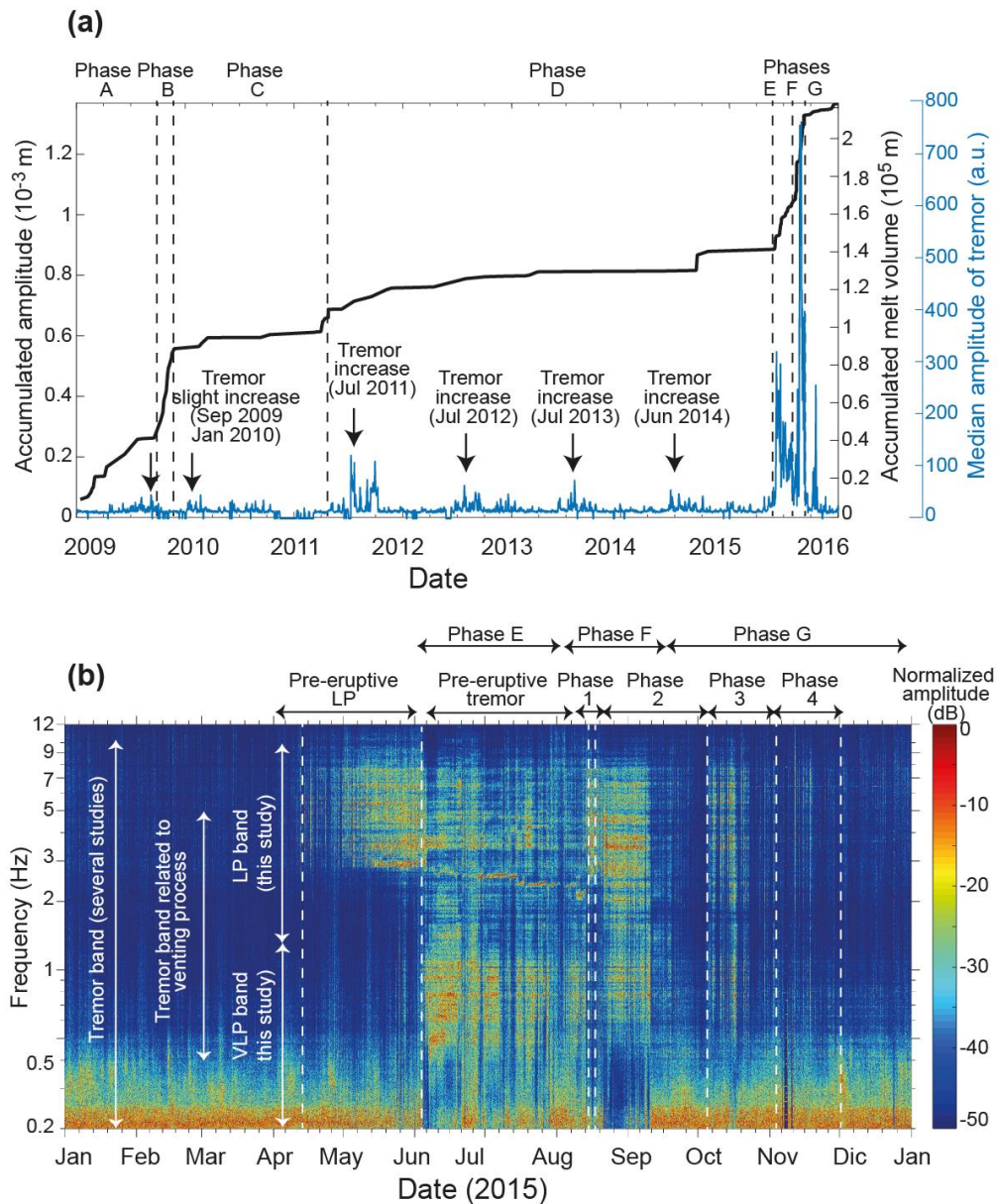
826

827

828

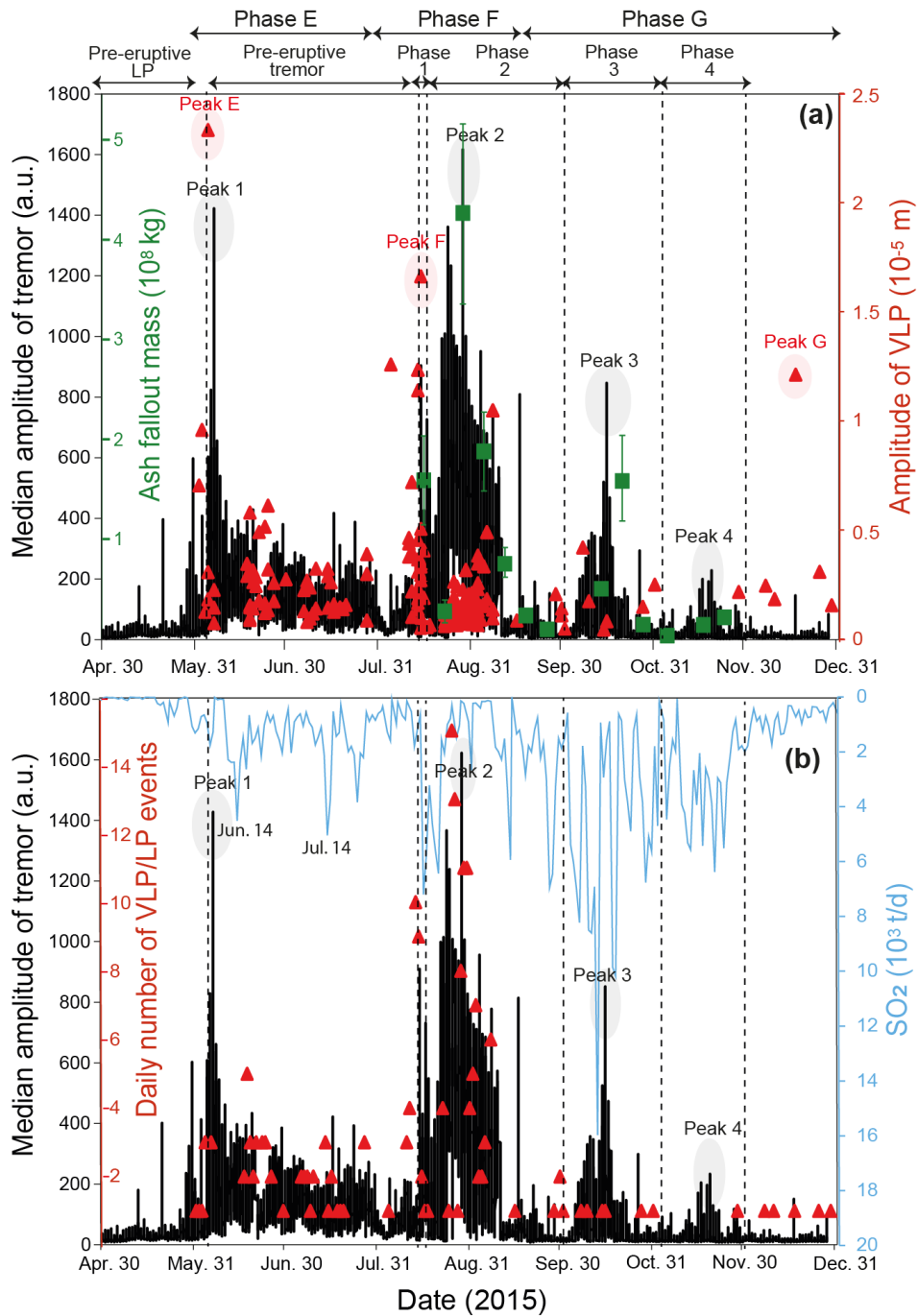
829

830



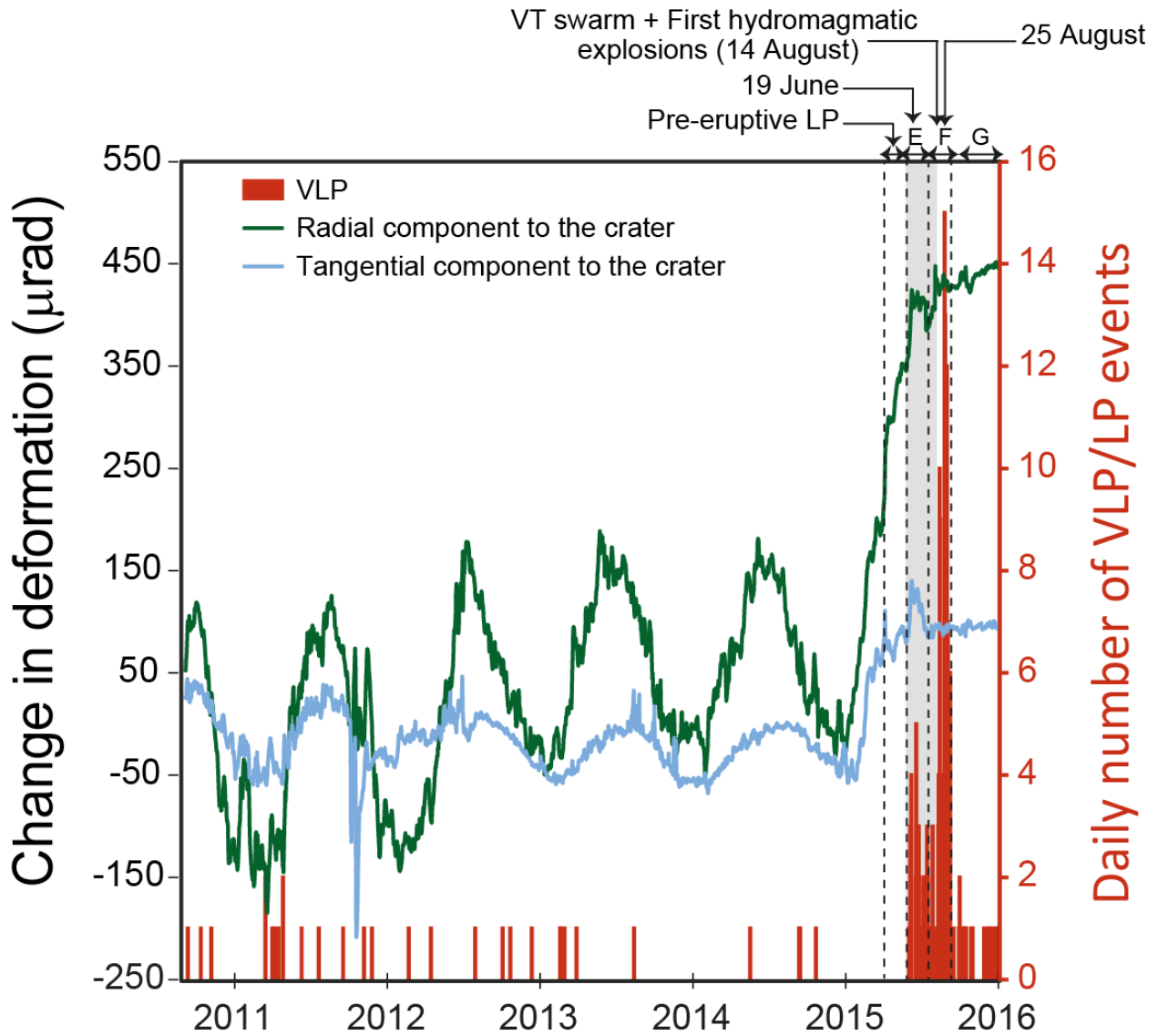
831

832 **Fig. 6.** (a) Accumulated amplitude and magma volume estimated of VLP signals in VLP/LP events
 833 in a frequency band of 0.08–0.5 Hz at BREF from 2009 to 2015 (see the text for details), overlapped
 834 with tremor amplitudes in arbitrary unit (a.u.). (b) Spectrogram of continuous vertical velocity
 835 waveform data at BREF between January and December 2015. Phases A–G were defined through
 836 the accumulated magma volume and VLP/LP activity. Phases 1–4 in (b) were defined by Bernard
 837 et al. (2016) based on tremor activity.

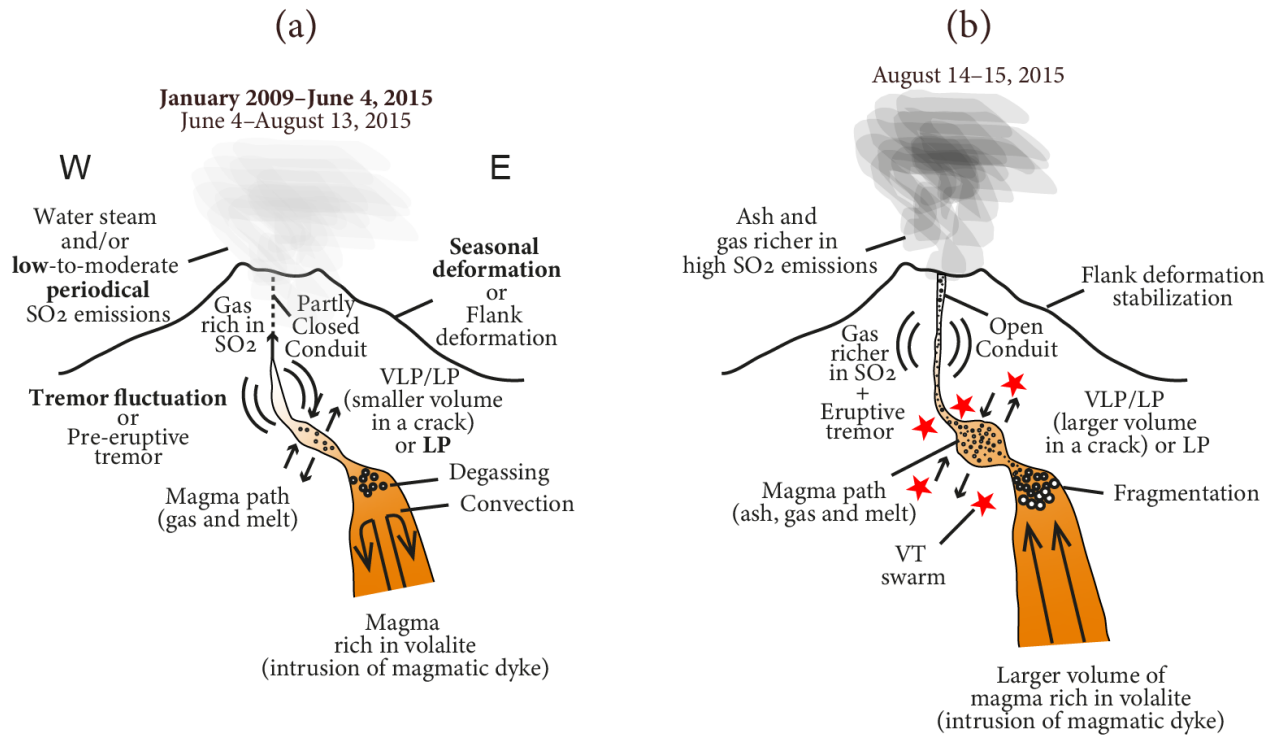


838

839 **Fig. 7.** Comparison of VLP/LP activity (red triangles) with tremor (black vertical bars), SO₂
 840 emission (blue lines), and ash fallout mass (green squares). Tremor amplitudes in arbitrary units
 841 (a.u.) and ash fallout mass are from Bernard et al. (2016), while SO₂ emission data are from Hidalgo
 842 et al. (2018) (online dataset at <https://ecl.earthchem.org/view.php?id=1165>). (a) Temporal
 843 variations in VLP amplitudes in VLP/LP events in the 0.08–0.5 Hz band, tremor amplitudes, and
 844 ash fallout mass. (b) Temporal variations in the daily number of VLP/LP events, tremor amplitudes,
 845 and SO₂ emission.



847
 848 **Fig. 8.** Temporal variations in ground deformation observed by the tiltmeter at VC1 (radial and
 849 tangential components to the crater shown by green and blue lines, respectively) and the daily
 850 number of VLP/LP events (red vertical bars). The period of pre-eruptive tremor is shown by gray
 851 area, and the first eruption on August 14 is indicated by an arrow. Peaks of VLP/LP activity on
 852 June 19 and August 25 are also shown by arrows. Vertical dashed lines emphasize the pre-eruptive
 853 LP events and phases E through G (see text for details).

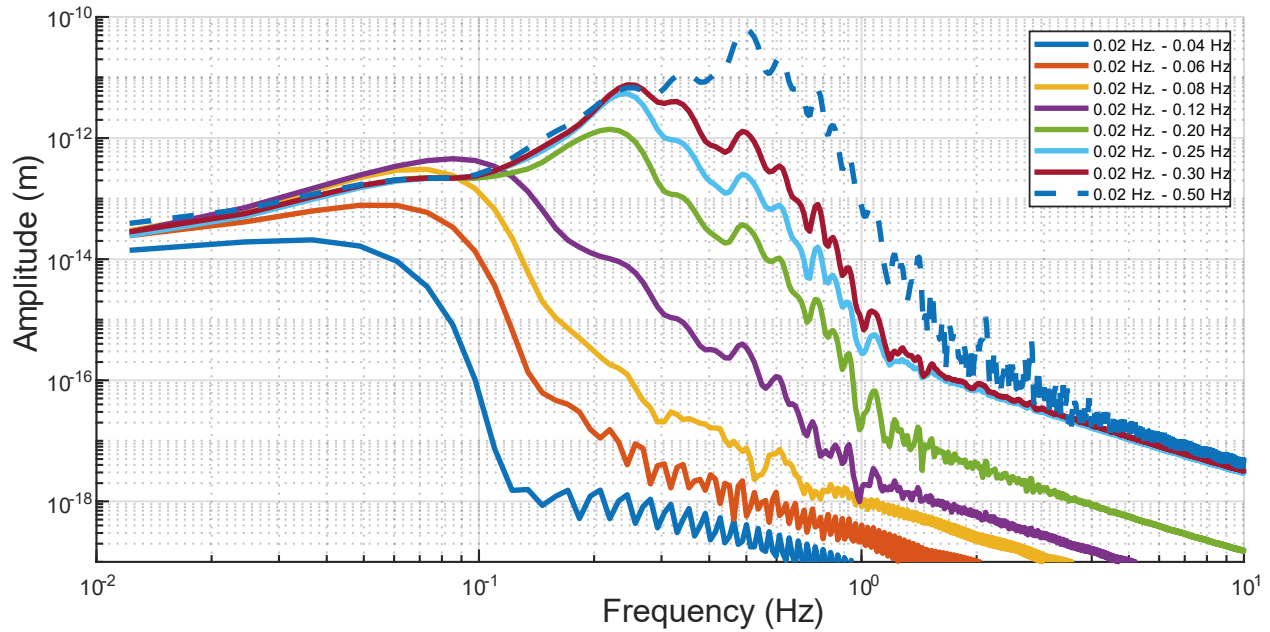


855
856 **Fig. 9.** Conceptual model for source processes of the VLP/LP events observed at Cotopaxi
857 Volcano. See Section 5 for details.

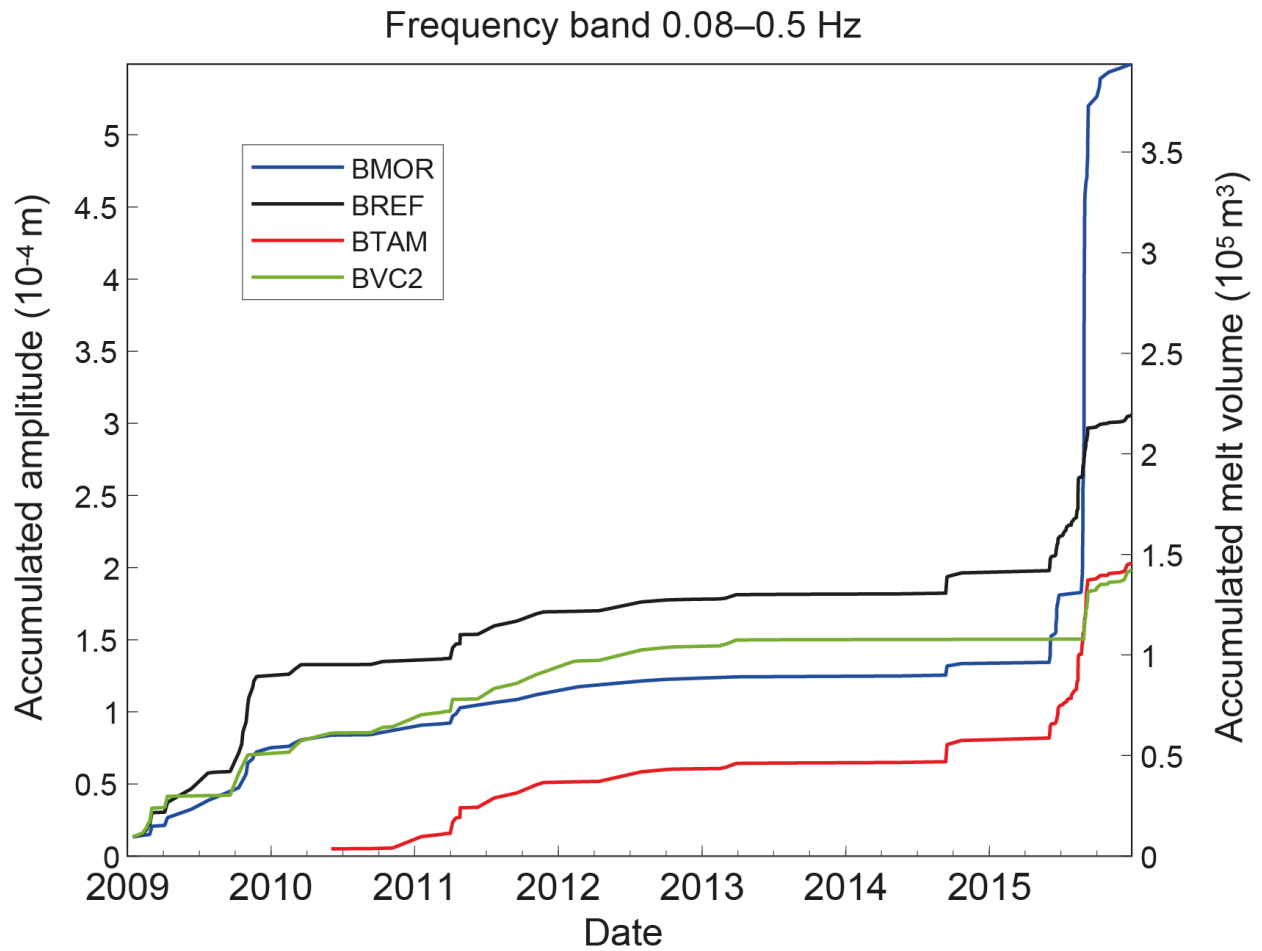
858

859 **SUPPORTING INFORMATION**

860 **Appendix A. Amplitude spectra of a VLP/LP event and accumulated amplitudes**
861 **and magma volumes.**



862
863 **Fig. A1.** Amplitude spectra of a VLP/LP event at Cotopaxi, band-passed with a Butterworth filter
864 at 8 distinct pass bands, with the low-frequency corner fixed in all instances (see legend). This
865 event occurred on January 14, 2009 at 18:54 and is the largest VLP/LP observed at Cotopaxi (see
866 text for details).



867
 868 **Fig. A2.** Accumulated amplitudes of VLP signals in VLP/LP events in a frequency band of
 869 0.08–0.5 Hz at the individual stations from 2009 to 2015 and accumulated magma volumes
 870 estimated from the accumulated amplitudes at the individual stations.

871